The LisbOn KInetics Monte Carlo solver

4 authors:

Tiago C. Dias
Technical University of Lisbon
4 PUBLICATIONS   **23** CITATIONS

L.L. Alves
Technical University of Lisbon
148 PUBLICATIONS   **2,292** CITATIONS

Antonio Tejero-del-Caz
University of Cordoba (Spain)
22 PUBLICATIONS   **251** CITATIONS

Vasco Guerra
Technical University of Lisbon
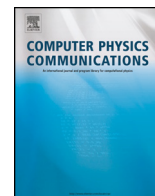**183** PUBLICATIONS   **4,171** CITATIONS

Some of the authors of this publication are also working on these related projects:

Project Advanced methane/CO2 conversion in DBD discharges View project

Project Wendelstein 7-X View project

The LisbOn KInetics Monte Carlo solver ☆,☆☆

Tiago C. Dias [a],*, Antonio Tejero-del-Caz [a,b], Luís L. Alves [a], Vasco Guerra [a]

[a] *Instituto de Plasmas e Fusão Nuclear, Instituto Superior Técnico, Universidade de Lisboa, Portugal*
[b] *Departamento de Física, Facultad de Ciencias, Universidad de Córdoba, Campus de Rabanales, Spain*

ARTICLE INFO

ABSTRACT

The LisbOn KInetics Monte Carlo (LoKI-MC) is an open-source simulation tool that solves the electron kinetics for low-temperature plasmas excited by uniform DC electric fields from different gas mixtures, using Monte Carlo techniques. Following the strategy and data organization of the LisbOn KInetics Boltzmann (LoKI-B) solver, the program easily addresses any complex mixture of atomic/molecular species, describing electron collisions with any target state (electronic, vibrational and rotational), characterized by any user-prescribed population. LoKI-MC is written in C++, benefiting from a highly-efficient object-oriented structure. On input, the code requires the working conditions, the gas-mixture composition, the distributions of populations for the levels of the atomic/molecular gases considered, and the relevant sets of electron-scattering cross sections obtained from the open-access website LXCat. On output, it yields the electron energy and velocity distribution functions, the electron swarm parameters, the collision rate-coefficients, and the electron power absorbed from the electric field and transferred to the different collisional channels. This paper presents LoKI-MC and gives examples of results obtained for different model and real gases, verifying and benchmarking the simulation tool against analytical solutions and other available codes, and assesses its computational performance. Moreover, the effects of the gas temperature, anisotropic ionization scattering (induced by momentum conservation) and superelastic collisions are analyzed in real gases.

Program summary

1. Introduction

Low-temperature plasmas (LTPs) are strongly reactive systems, characterized by a low density of charged particles (ionization degrees $\sim 10^{-6} - 10^{-3}$), high electron temperature (~ 1 eV) and heavy-species translational and internal temperatures ranging from 300 K to $\sim 10^4$ K. The strong non-equilibrium nature of LTPs can efficiently stimulate several chemical processes relevant for industrial [1,2], medical [3–5], agricultural [6–8] and environmental [9,10] applications. Electrons play a major role in these plasmas, since they transmit the energy acquired from the electric field to the heavy particles through various collisional channels, thereby enhancing the reactivity of the environment. Therefore, the taming and tuning of the energy distribution of the electrons is essential to maximize the capability of LTPs.

The electron kinetics in gas discharges can be described in detail by solving numerically the differential electron Boltzmann equation (EBE), or by tracking the stochastic motion of the individual electrons using Monte Carlo methods [11]. Publicly available simulation tools based on either approach were developed in the last decades, for the benefit of the LTP community. Some exam-

---

ples are ELENDIF [12], BOLSIG+ [13], EEDF [14], BOLOS [15], LoKI-B [16,17], MultiBolt [18], METHES [19] and Magboltz [20], the latter five being open-source codes. The first five codes rely on a low-anisotropy approximation, keeping only two terms in an expansion of the electron distribution in Legendre polynomials over the velocity space [21]. Multibolt is a multi-term Boltzmann equation solver and METHES is a Monte Carlo collision code [22], both written in MATLAB. Magboltz is a Fortran code that uses a Monte Carlo integration technique for solving the EBE. BOLSIG+, BOLOS, LoKI-B, MultiBolt and METHES accept input files with electron scattering cross sections obtained from the LXCat open-access website [23]. The LisbOn KInetics Boltzmann solver (LoKI-B) was developed as a response to the need of having an electron Boltzmann solver easily addressing the simulation of the electron kinetics in any complex gas mixture of atomic/molecular species, describing electron collisions with any target state (electronic, vibrational and rotational), characterized by any user-prescribed population, and accounting for superelastic and stepwise excitation processes.

The range of reduced electric fields E/N (the ratio of the electric field to the gas density) where the two-term approximation is valid strongly depends on the background gas mixture and, without benchmark with more accurate formulations, one can never be sure about the accuracy of this approach [24–27]. Nevertheless, in all gases the two-term approximation fails for sufficiently high values of E/N, as strong electric fields induce a preferential direction in the electron motion, thus leading to important anisotropies. Multibolt, as multi-term solver, and METHES and Magboltz, as Monte Carlo solvers, do not have this drawback. However, Magboltz uses hardcoded cross sections. Furthermore, Multibolt and METHES do not consider the thermal motion of the background gas molecules, and do not address the internal levels of the atoms/molecules nor superelastic collisions.

It is clear that the community is still lacking a general and flexible Boltzmann equation solver that does not depend on the two-term approximation. This work presents the LisbOn KInetics Monte Carlo (LoKI-MC) open-source code, which solves the electron transport in a gas subject to an uniform DC electric field using Monte Carlo techniques. LoKI-MC is written in C++, benefiting from an efficient object-oriented structure, and follows the data organization of LoKI-B. Compared with the previously mentioned open-source codes that do not use the two-term expansion, the solver presented in this paper has the following advantages: (i) inclusion of the thermal motion of the gas molecules, allowing to describe the electron swarms at low E/N and to obtain the correct thermodynamic properties in the limit of vanishingly small fields; (ii) straightforward insertion of gas internal levels (electronic, vibrational and rotational) and, accordingly, of superelastic and stepwise processes; (iii) possibility of describing anisotropic scattering in ionization, induced by momentum conservation, and availability of different models for the energy sharing between primary and secondary electrons; (iv) calculation of the electron power balance, available on output; (v) provision of the higher-order anisotropies of the distribution function.

Another strong motivation for this work is the creation of a self-consistent and unified formulation of plasma-chemistry based on Kinetic Monte Carlo (KMC) techniques [28]. The typical plasma-chemistry models, based on the low-anisotropy and quasi-stationary approximations to the electron energy distribution function, may fail to describe fast-pulsed discharges correctly due to the high reduced electric fields and very short timescales involved [17,29–34]. A simultaneous KMC description of the electron and heavy-species kinetics would enable a rigorous inclusion of the time-dependent influence of different excited states in the electron kinetics and vice-versa, and would not be limited to a restricted range of E/N. Such program was initiated in [28] with the development of a powerful KMC description of the heavy-particle

kinetics. LoKI-MC is designed to be easily integrated in this kind of formulation.

This paper is organized as follows. Section 2 discusses in detail the Monte Carlo formalism adopted to study the electron kinetics. Section 3 summarizes the scope of the LoKI-MC code, focusing on the required input data and the possible output information. Section 4 presents an extensive verification and benchmarking in model gases and real gases, and discusses the influence of anisotropic ionization scattering and superelastic collisions on the results. Section 5 closes the work with final remarks and future guidelines.

2. Methods

The Monte Carlo method presented here consists on the study of the electron transport in a background gas, under the influence of an uniform DC electric field **E**, by following the stochastic trajectory of a representative ensemble of N_e electrons. Electrons move in an unbounded environment, performing series of free flights interrupted by elastic, inelastic or superelastic collisions with gas molecules. The collision-free times and the collision dynamics are calculated by generating random numbers sampled from probability distributions based on the underlying physics. In the first code release, with the exception of ionization, electron collisions are assumed isotropic. The random numbers are produced with a 64-bit version of the Mersenne Twister pseudorandom number generator using the function `mt19937_64` implemented at the C++ library `random` [35–37], which is characterized by a high period and good uniformity. During the simulation, the information of the electrons is stored in order to calculate distribution functions, transport coefficients and other relevant quantities.

2.1. Cross sections

The momentum-transfer cross section for an electron-neutral collision, described by a differential (angle-resolved) cross section $\sigma(\epsilon, \theta)$, is generally defined as [38]

$$\sigma_c(\epsilon) \equiv \frac{1}{2} \int_0^\pi \sigma(\epsilon, \theta)(1 - \cos\theta)\sin\theta d\theta . \tag{1}$$

For a gas k, the electron-neutral momentum-transfer cross section $\sigma_{k,c}(\epsilon)$ is constructed by weighting the contributions of the different types of collisional mechanisms to give [16]

$$\sigma_{k,c}(\epsilon) = \sum_i \xi_{k_i} \sigma_{k_i,c}^{\text{el}}(\epsilon) + \sum_{i,j>i} \left[\xi_{k_i} \sigma_{k_{(i,j)},c}(\epsilon) + \xi_{k_j} \sigma_{k_{(j,i)},c}(\epsilon) \right], \tag{2}$$

where ξ_{k_i} is the fractional population of the level k_i; $\sigma_{k_i,c}^{\text{el}}$, $\sigma_{k_{(i,j)},c}$ and $\sigma_{k_{(j,i)},c}$ are the electron-neutral momentum-transfer cross sections for the elastic scattering of level k_i, the inelastic excitation $k_i \to k_j$, and the superelastic de-excitation $k_j \to k_i$, respectively. The latter cross sections are frequently taken assuming an *isotropic scattering*, in which case one can identify the momentum-transfer cross section with the integral cross section $\sigma_{k_{(i,j)}}$ (integrated over all scattering angles), i.e., $\sigma_{k_{(i,j)},c} \simeq \sigma_{k_{(i,j)}}$. Moreover, the elastic momentum-transfer is usually identified with that of the highly-populated ground-state of the gas, which amounts to assume the same momentum-transfer cross section for all states of the gas. Therefore,

$$\sigma_{k,c}(\epsilon) \simeq \sigma_{k,c}^{\text{el}}(\epsilon) + \sum_{i,j>i} \left[\xi_{k_i} \sigma_{k_{(i,j)}}(\epsilon) + \xi_{k_j} \sigma_{k_{(j,i)}}(\epsilon) \right]. \tag{3}$$

In some cases, the elastic momentum-transfer cross section is not available and only the total momentum-transfer cross section is known, which in databases is usually termed as *effective* $\sigma_{k,c}^{\text{eff}}$. In such cases, the elastic component can be deduced by subtracting the inelastic and superelastic contributions

$$\sigma_{k,c}^{\text{el}}(\epsilon) = \sigma_{k,c}^{\text{eff}}(\epsilon) - \sum_{i,j>i} \left[\xi_{k_i}^{\text{prescribed}} \sigma_{k_{(i,j)}}(\epsilon) + \xi_{k_j}^{\text{prescribed}} \sigma_{k_{(j,i)}}(\epsilon) \right],$$

where the populations $\xi_{k_i}^{\text{prescribed}}$ and $\xi_{k_j}^{\text{prescribed}}$ correspond to some prescribed distribution, coherent with the measured/estimated data of $\sigma_{k,c}^{\text{eff}}$, and allowing to obtain a *unique* result (density independent) for the elastic cross section [16]. By default, LoKI-MC adopts a Boltzmann distribution at the room temperature for $\xi_{k_i}^{\text{prescribed}}$. We recommend to replace, whenever possible, the data for effective momentum-transfer cross sections with that for elastic momentum-transfer cross sections.

The cross-section values are matched to an energy grid by linear interpolation [16]. Following the ontology of separating the data from the code, no extrapolation is made for energies larger than the maximum energy of the provided cross section. The maximum energy of the grid is updated dynamically along the simulation depending on the energy of the electron ensemble.

Finally, the cross sections of the superelastic processes $k_j \rightarrow k_i$ are determined from the Klein-Rosseland relation, expressing the principle of detailed balance [39]:

$$\sigma_{k_{(j,i)}}(\epsilon) = \frac{g_{k_i}}{g_{k_j}} \frac{\epsilon + \Delta\epsilon_{k_{(i,j)}}}{\epsilon} \sigma_{k_{(i,j)}}(\epsilon + \Delta\epsilon_{k_{(i,j)}}),$$ (4)

where g_{k_i} and g_{k_j} denote the statistical weights of the levels k_i and k_j, respectively, and $\Delta\epsilon_{k_{(i,j)}}$ is the energy threshold of the inelastic collision $k_i \rightarrow k_j$.

2.2. Free flight

To describe the free flight of an electron, we need to determine when the next collision will occur. This can be done using either the integration method [40] or the null collision technique introduced by Skullerud [41]. We employ the latter, where the times between collisions are calculated without any numerical integration through the use of a constant trial collision frequency ν' which must satisfy

$$\nu' \geq \max_{\text{all } v_r} \{\nu_T(v_r)\},$$ (5)

where $\nu_T(v_r)$ is the total collision frequency for a given relative speed $v_r = |\mathbf{v} - \mathbf{V}|$, and $\mathbf{v}$ and $\mathbf{V}$ are the velocities of the incident electron and the target molecule, respectively. In this case, the distribution of collision times t_c is exponential: $P(t_c) = \nu' \exp(-\nu' t_c)$. Using simple theorems of probability theory, the time between two successive collisions can be obtained by generating an uniform random number p_t in the]0,1[range [42]:

$$t_c = -\frac{\ln(p_t)}{\nu'}.$$ (6)

Pay attention that $p_t = 0$ or 1 are excluded to avoid an infinite or null collision time, respectively. Effectively, with the null collision technique, we introduce another collisional process (where no real interaction occurs) with a collision frequency which, when added to the total collision frequency $\nu_T(v_r)$, gives a constant value ν' for all relative speeds v_r.

Having determined the collision time t_c, the position $\mathbf{r}$ and velocity $\mathbf{v}$ of the N_e electrons at the end of the free flight are calculated by integrating analytically the classical equations of motion:
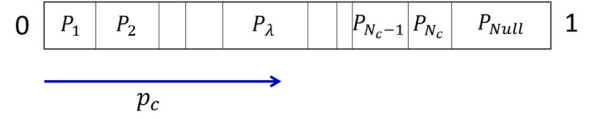

Fig. 1. Selection of the collision type.

$$\mathbf{r}(t + t_c) = \mathbf{r}(t) + \mathbf{v}(t)t_c - \frac{e\mathbf{E}}{2m}t_c^2,$$ (7)

$$\mathbf{v}(t + t_c) = \mathbf{v}(t) - \frac{e\mathbf{E}}{m}t_c,$$ (8)

where e and m are the electron charge and mass, respectively. Note that, in LoKI-MC, the electric field $\mathbf{E}$ is antiparallel to the z axis ($\mathbf{E} = -E\hat{\mathbf{z}}$). Additionally, all electrons are advanced with the same time-step t_c, as in METHES [19]. Thus, in spite of t_c being randomly generated for each free-flight, the assigned value is the same for all electrons. The synchronous advance of electrons strongly facilitates the sampling of the electron ensemble and will be essential when coupling LoKI-MC with the temporal evolution of the chemical kinetics, to be done in future works. Finally, we should mention that the Leapfrog/Velocity-Verlet method is used very often to integrate the equations of motion in space- and time-varying fields (see e.g. [43]). However, in this case such approach is not needed since we are dealing with an uniform DC electric field, and equations (7) and (8) are the exact solution of the motion.

2.3. Collision choice

After propagating the electrons during the free flight, we should determine the type of electron-neutral collision that each of them undergoes. The likelihood of the occurrence of a collision of kind $\mathcal{K}$, out of the N_c kinds available, is proportional to the corresponding collision frequency $\nu_{\mathcal{K}}$:

$$P_{\mathcal{K}} = \frac{\nu_{\mathcal{K}}(v_r)}{\nu'} = \frac{n_{\mathcal{K}}^s \sigma_{\mathcal{K}}(v_r) v_r}{\nu'}.$$ (9)

Here, $n_{\mathcal{K}}^s$ is the density of the target species s and $\sigma_{\mathcal{K}}(v_r)$ is the collision cross section. The relative speed v_r requires the knowledge of the target velocity $\mathbf{V}$, which is determined from a Maxwell-Boltzmann distribution at the gas temperature. Moreover, considering the overestimation of the collision frequency in the calculation of the free-flight time, expressed by equation (5), we add a null collision process with probability $P_{\text{null}} = \frac{\nu_{\text{null}}(v_r)}{\nu'} = \frac{\nu' - \nu_T(v_r)}{\nu'}$. Based on the generation of a random number $p_c \in]0,1]$, the collision kind is chosen as illustrated in Fig. 1:

- if $p_c \leq \sum_{\mathcal{K}=1}^{N_c} P_{\mathcal{K}}$, choose the collision kind λ for which $\sum_{\mathcal{K}=1}^{\lambda-1} P_{\mathcal{K}} < p_c \leq \sum_{\mathcal{K}=1}^{\lambda} P_{\mathcal{K}}$;
- else, the collision is null.

This procedure is repeated for each electron.

The collisions chosen for each electron are then performed. To do so, we admit that the collisions are local ($\mathbf{r} = \mathbf{r}'$) and instantaneous ($t = t'$), where $'$ means "immediately after the collision". The electrons undergoing null collisions have no velocity changes ($\mathbf{v} = \mathbf{v}'$). The velocity changes during real electron-neutral collisions depend on their type, as discussed in the following couple of sections.

2.4. Conservative collisions

For the treatment of conservative collisions, we mainly follow the work of Yousfi et al. [44], where the influence of the non-null

target velocity is considered and isotropic scattering is assumed. The electron velocity after the collision, $\mathbf{v}'$, is determined from the conservation equation of momentum transfer in the laboratory frame,

$$\mathbf{v}' = \frac{M}{m_e + M}\mathbf{v}'_{\mathbf{r}} + \frac{m_e\mathbf{v} + M\mathbf{V}}{m_e + M}, \tag{10}$$

where M is the mass of the neutral heavy-species. The second term of the right-hand side represents the velocity of the center-of-mass frame, which is known. Thus, we only need to determine the relative velocity after the collision $\mathbf{v}'_{\mathbf{r}}$.

The relative speed v'_r is calculated from energy conservation:

$$v'_r = \left[v_r^2 - \frac{2}{\mu} E_{\text{loss}} \right]^{1/2}, \tag{11}$$

where E_{loss} represents the energy lost in the collision, which is zero, positive or negative, if the collision is elastic, inelastic or superelastic, respectively; $\mu = m_e M/(m_e + M)$ is the reduced mass of the system electron + molecule.

The direction of the relative velocity $\mathbf{v}'_{\mathbf{r}}$ is determined in the center-of-mass frame from the calculation of the scattering angle χ' and the azimuthal angle η'. The scattering angle $\chi' \in [0, \pi]$ consists on the angle between $\mathbf{v}'_{\mathbf{r}}$ and $\mathbf{v}_{\mathbf{r}}$. Assuming *isotropic scattering*, this angle is calculated from an uniform distribution of random numbers $p_\chi \in [0, 1]$:

$$\chi' = \arccos(1 - 2p_\chi). \tag{12}$$

Similarly, the azimuthal angle η' is calculated with another random number $p_\eta \in]0, 1]$:

$$\eta' = 2\pi p_\eta, \tag{13}$$

where we assume that η' is uniformly distributed in $]0, 2\pi]$.

The knowledge of the relative speed v'_r together with the angles χ' and η' defines the relative velocity $\mathbf{v}'_{\mathbf{r}}$ in the center-of-mass frame. Using the well-known Euler relations, this vector is projected into the laboratory frame according to

$$\begin{cases} v'_{rx} = v'_r(-\sin\chi'\sin\eta'\sin\phi_r + \sin\chi'\cos\eta'\cos\theta_r\cos\phi_r \\ \qquad\qquad + \cos\chi'\sin\theta_r\cos\phi_r) \\ v'_{ry} = v'_r(\sin\chi'\sin\eta'\cos\phi_r + \sin\chi'\cos\eta'\cos\theta_r\sin\phi_r \\ \qquad\qquad + \cos\chi'\sin\theta_r\sin\phi_r) \\ v'_{rz} = v'_r(-\sin\chi'\cos\eta'\sin\theta_r + \cos\chi'\cos\theta_r) \end{cases}, \tag{14}$$

where θ_r is the polar angle and ϕ_r is the azimuthal angle in the laboratory frame of vector $\mathbf{v}_{\mathbf{r}}$. Finally, using equation (10), the electron velocity after the collision $\mathbf{v}'$ is calculated in the laboratory frame.

A very common approximation involves neglecting the molecular motion, since the mass of the electron is much smaller than that of the molecule ($m_e + M \simeq M$). In this case, the electron speed after the collision is [45]

$$v' = \left\{ \left(v^2 - \frac{2E_{loss}}{m_e} \right) \left[1 - \frac{2m_e M}{(m_e + M)^2}(1 - \cos\chi') \right] \right\}^{1/2}, \tag{15}$$

and the velocity $\mathbf{v}'$ is determined in the laboratory frame after generating the scattering angles and applying them in the Euler relations.

In LoKI-MC, it is possible to choose between the approximative treatment of (15), or preserving the effect of the gas temperature calculating relative velocities from (10)-(11). Furthermore, to improve the computational efficiency while ensuring a correct treatment for low electron energies, it is also possible to choose a

hybrid solution where the molecular motion is taken into account only when the electron energy ϵ is comparable to the gas mean energy: $\epsilon \leq 20 \times \frac{3}{2}k_B T_g$, where k_B is the Boltzmann constant and T_g is the gas temperature. This constitutes a very good approach since, even when the electron and molecule energies are similar, the electron speed is much larger than the molecule speed, due to a much lower mass.

2.5. Non-conservative collisions

We consider two types of non-conservative processes: attachment and ionization. In attachment, the electron is simply removed from the simulation. In ionization, the dynamics is more complex since it involves three bodies. However, as the ionization energy is much higher than the gas thermal energy, considering target molecules at rest is a very good approximation in the treatment of ionization, which strongly simplifies the calculations. Following this approach, the energies of the scattered (ϵ') and ejected (ϵ_{ej}) electrons are restrained by

$$\epsilon' + \epsilon_{\text{ej}} = \epsilon - \Delta\epsilon_{\text{ion}}, \tag{16}$$

where ϵ is the incident electron energy and $\Delta\epsilon_{\text{ion}}$ is the ionization potential.

Upon the knowledge of the single differential ionization cross section (SDCS) $\sigma_{\text{ion}}(\epsilon, u)$, the energy of one electron (for instance, the ejected electron) can be obtained from a unit uniform distribution of random numbers p_{ion} using [46]

$$p_{\text{ion}} = \frac{\int_0^{\epsilon_{ej}} \sigma_{\text{ion}}^{\text{ej}}(\epsilon, u)du}{\sigma_{\text{ion}}(\epsilon)}, \tag{17}$$

where $\sigma_{\text{ion}}(\epsilon)$ is the integral ionization cross section. This equation is solved to find ϵ_{ej} and the energy of the scattered electron ϵ' is calculated from the conservation equation (16). We use a fitting expression for the SDCS proposed by Opal et al. based on a comprehensive set of measurements [47,48]:

$$\sigma_{\text{ion}}^{\text{ej}}(\epsilon, u) = \frac{\sigma_{\text{ion}}(\epsilon)}{w \arctan[(\epsilon - \Delta\epsilon_{\text{ion}})/(2w)]} \frac{1}{1 + (u/w)^\beta}, \tag{18}$$

where $\beta \simeq 2$ and w is a parameter close to the ionization threshold $\Delta\epsilon_{\text{ion}}$, which is set for each gas according to the original estimates. Alternatively, when the differential ionization cross section is not known, we can assume a fixed energy sharing factor γ between the two electrons: $\epsilon_{ej} = \gamma(\epsilon - \Delta\epsilon_{\text{ion}})$. For $\gamma = 0.5$, there is equal energy sharing; for $\gamma = 0$, the scattered electron takes all the residual energy.

With the energies (and speeds) of the two electrons determined, it is still necessary to define the directions of the velocities. One possibility is to assume isotropic scattering for both electrons using equations similar to (12) and (13). However, in this situation the linear momentum is not conserved. In fact, the general problem is undetermined and two additional assumptions may be taken as an alternative to isotropic scattering [49]: the incident, ejected and scattered electron velocities are coplanar; the scattered and ejected electron velocities are perpendicular. Considering the conservation of energy and momentum, these assumptions lead to [49]:

$$\cos\chi' = \sqrt{\frac{\epsilon'}{\epsilon - \epsilon_{\text{ion}}}}, \tag{19a}$$

$$\cos\chi_{\text{ej}} = \sqrt{\frac{\epsilon_{\text{ej}}}{\epsilon - \epsilon_{\text{ion}}}}. \tag{19b}$$

The azimuthal angle of the scattered electron is determined assuming a uniform distribution in $]0, 2\pi]$: $\eta' = 2\pi p_\eta$. The azimuthal angle of the ejected electron is $\eta_{\text{ej}} = \eta' + \pi$. Finally, the velocities of the scattered ($\mathbf{v}'$) and ejected ($\mathbf{v}_{\text{ej}}$) electrons are obtained in the laboratory frame using Euler transformations similar to the relations (14).

In LoKI-MC, the ionization scattering can be defined to be either isotropic or anisotropic (induced by momentum conservation). This flexibility is important since most Boltzmann solvers assume isotropic scattering in ionization and the cross-section sets are usually optimized in this condition (see section 4.4). Moreover, the user can choose the model for energy sharing between primary and secondary electrons: equal energy, one electron takes all, or the SDCS proposed by Opal et al. [47], where in the latter case the parameter ω must be provided.

The number of electrons N_e in the simulation is fixed to a constant value using the particle-replacement method, which is frequently applied by the scientific community and does not affect the average properties of the ensemble [19,50–52]. This technique was extensively analyzed by Mirić et al. [52] and Rabie and Franck [19], in conditions where non-conservative processes have a strong influence. In the case of ionization, the ejected electron is created and a randomly chosen electron is removed from the ensemble. In an attachment collision, the incident electron is removed and this lost is compensated by copying a random electron from the ensemble. The employed strategy confers stability to the code, since it avoids the exponential increase of electrons in conditions of strong ionization, which would significantly degrade the computational times, and the loss of most electrons in a simulation with pronounced attachment. Take note that another valid approach would be to use a dynamical particle list, whose size grows/decreases depending on ionization/attachment events, and remove/copy electrons only when the total number of electrons lies outside of a defined interval [53,54].

2.6. Data sampling

After the electron swarm reaches a steady-state, the positions $\mathbf{r}$ and velocities $\mathbf{v}$ of the electrons are sampled along time in order to calculate the electron transport properties: mean energy, distribution functions, transport parameters, collision rates and power balance. The steady-state time t_{ss} is considered automatically when the swarm energy (average over the ensemble of electrons) is constant apart from statistical fluctuations, which is verified when two conditions are fulfilled: the temporal average of the swarm energy in the interval $[0.5t, 0.75t]$ is larger than the one in the interval $[0.75t, t]$; the relative standard deviation of the temporal average in the latter interval is smaller than 1%. An example of the temporal evolution of the swarm energy and the corresponding steady-state time is shown in Fig. 2.

To acquire as much statistics as possible, the sampling is always done after each electron free-flight. Since each sampling time is not statistically independent, the standard deviation of the mean value should be determined with care. We divide the manifold of statistical points in 50 subgroups and calculate the mean value of each one. Then, the statistical error of the total mean value is estimated through the dispersion of the 50 mean values calculated. For example, if the simulation describes 10^5 free flights after the steady-state is reached, the number of points between subgroup centers is $10^5/50 = 2000$.

2.6.1. Electron mean energy and distribution functions

The mean energy $\langle \epsilon \rangle$ is calculated by averaging the kinetic energies $\epsilon_{\alpha\beta}$ of the N_e electrons during N_{int} integration points
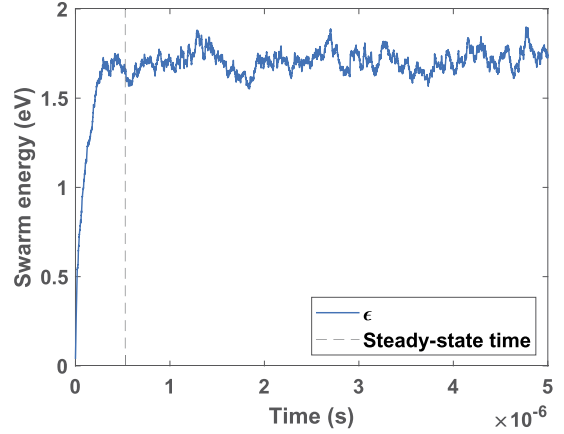

Fig. 2. Example of the temporal evolution of the swarm energy (O_2, $E/N = 10$ Td, $p = 133.32$ Pa, $T_g = 300$ K). In this case, the steady-state time is $\simeq 0.54$ µs.

$$\langle \epsilon \rangle = \frac{1}{N_{\text{int}} N_e} \sum_{\alpha=1}^{N_{\text{int}}} \sum_{\beta=1}^{N_e} \epsilon_{\alpha\beta} \, . \tag{20}$$

One of the most meaningful quantities extractable from the Monte Carlo simulations is the electron energy distribution function (EEDF). For comparison with other codes that solve the electron Boltzmann equation in a deterministic way, we calculate not only the EEDF, but also the different anisotropies of the electron distribution function, following its usual decomposition in a series of Legendre polynomials $P_l(\cos\theta)$ with $l = 0, 1, ...$, where θ is the angle between $\mathbf{v}$ and the direction of the anisotropy (in this case defined exclusively by the electric field).

Concerning the EEDF calculation, let the energies be discretized into $\mathcal{N}_E$ cells of energies $\{E_1, ..., E_m, ..., E_{\mathcal{N}_E}\}$, with constant energy step $\Delta_E = E_{m+1} - E_m$. Similarly to the mean energy, the EEDF is calculated by averaging over all electrons and all integration points [44]:

$$f_0(E_m) = \frac{\sum_{\alpha=1}^{N_{\text{int}}} \sum_{\beta=1}^{N_e} \delta(\epsilon_{\alpha\beta})}{N_{\text{int}} N_e \sqrt{E_m} \Delta_E} \, , \tag{21}$$

where

$$\delta(\epsilon_{\alpha\beta}) = \begin{cases} 1, & \text{if } E_m - \frac{\Delta_E}{2} \leq \epsilon_{\alpha\beta} < E_m + \frac{\Delta_E}{2} \\ 0, & \text{otherwise} \end{cases} \, .$$

Note that the EEDF is normalized as to satisfy $\sum_{m=1}^{\mathcal{N}_E} f_0(E_m) \sqrt{E_m} \Delta_E = 1$. By default, the energies in LoKI-MC are discretized into $\mathcal{N}_E = 500$ cells.

To obtain the higher-order anisotropies, we first calculate the electron angular distribution function $f(E_m, \cos\Theta_n)$, which requires a discretization on the angles: $\{\cos\Theta_1, ..., \cos\Theta_n, ..., \cos\Theta_{\mathcal{N}_\Theta}\}$, with constant step $\Delta_\Theta = \cos\Theta_{n+1} - \cos\Theta_n$. The angular distribution function is discretized as follows:

$$f(E_m, \cos\Theta_n) = \frac{2 \sum_{\alpha=1}^{N_{\text{int}}} \sum_{\beta=1}^{N_e} \delta(\epsilon_{\alpha\beta}, \cos\theta_{\alpha\beta})}{N_{\text{int}} N_e \sqrt{E_m} \Delta_E \Delta_\Theta} \, , \tag{22}$$

where

$$\delta(\epsilon_{\alpha\beta}, \cos\theta_{\alpha\beta})$$

$$= \begin{cases} 1, & \text{if } \begin{aligned} &E_m - \frac{\Delta_E}{2} \leq \epsilon_{\alpha\beta} < E_m + \frac{\Delta_E}{2} \text{ and} \\ &\cos\Theta_n - \frac{\Delta_\Theta}{2} \leq \cos\theta_{\alpha\beta} < \cos\Theta_n + \frac{\Delta_\Theta}{2} \end{aligned} \, , \\ 0, & \text{otherwise} \end{cases}$$
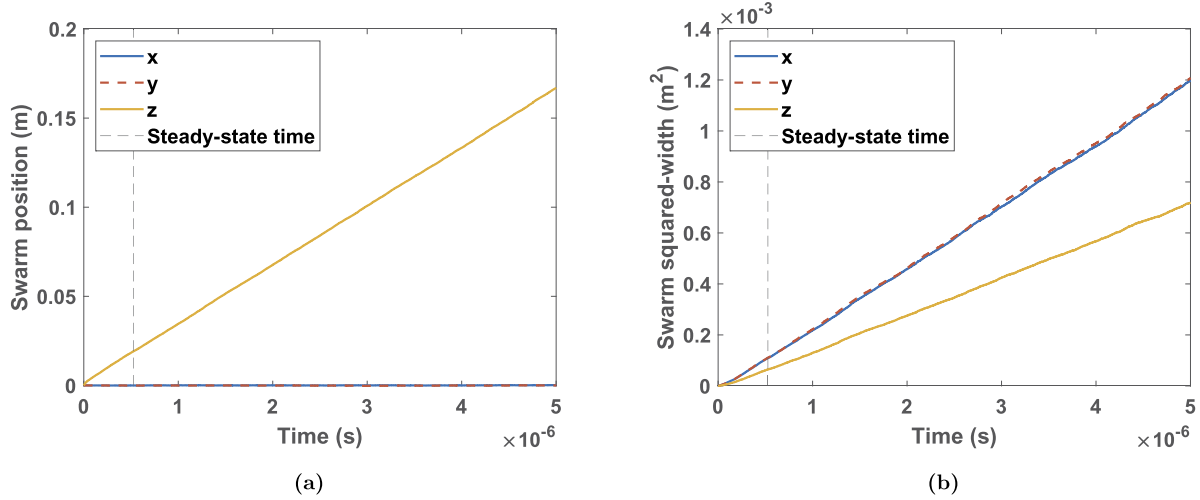
Fig. 3. Example of the temporal evolution of the swarm mean position (a) and mean squared width (b), in the same conditions as Fig. 2. The bulk transport parameters are determined from the slopes of the lines (see text).

and is normalized as to satisfy $\frac{1}{2} \sum_{m=1}^{\mathcal{N}_E} \sum_{n=1}^{\mathcal{N}_\Theta} f(E_m, \cos \Theta_n) \sqrt{E_m} \Delta_E \Delta_\Theta$ $= 1$. Then, the anisotropies $f_l(E_m)$ are determined from [55]

$$f_l(E_m) = \frac{2l+1}{2} \sum_{n=1}^{\mathcal{N}_\Theta} P_l(\cos \Theta_n) f(E_m, \cos \Theta_n) \Delta_\Theta . \tag{23}$$

By default, the angles are discretized into $\mathcal{N}_\Theta = 50$ cells.

Finally, the electron velocity distribution function (EVDF) is determined in a similar way through a discretization of the radial ($v_{r,m}$) and axial ($v_{z,n}$) velocity space, ensuring that $f(v_r, v_z)$ verifies $\int_0^\infty 2\pi v_r dv_r \int_{-\infty}^{+\infty} dv_z f(v_r, v_z) = 1$. By default, the velocity space is discretized using 200 cells for both the radial and the axial components.

2.6.2. Electron-impact rate coefficients

The electron-impact rate coefficients $k_\mathcal{K}$ are determined using two methods. The direct way is to count the collision events of type $\mathcal{K}$ per electron during the sampling time $t - t_{ss}$, $C_\mathcal{K}/N_e$ [51, 56]:

$$k_\mathcal{K} = \frac{1}{t - t_s} \frac{C_\mathcal{K}/N_e}{n_\mathcal{K}^s} . \tag{24}$$

However, when the density of the target species $n_\mathcal{K}^s$ is too low, the result is statistically imprecise due to the low number of events during the simulation. The second approach relies only on the convolution of the EEDF with the collision cross section:

$$k_\mathcal{K} = \sqrt{\frac{2e}{m_e}} \int_0^\infty \sigma_\mathcal{K}(\epsilon) \epsilon f_0(\epsilon) d\epsilon . \tag{25}$$

Both methods are correct but the latter should be preferred to obtain the steady-state rate-coefficients, since it depends only on the quality of the EEDF, regardless of the target densities used in the simulation.

2.6.3. Transport parameters

For the determination of the transport parameters, we distinguish between "flux" and "bulk" components, which may differ when non-conservative processes are significant [56].

The flux drift velocity $\mathbf{v_d^f}$ and diffusion coefficient $\mathbf{D^f}$ are determined by averaging over all *electron trajectories* during the integration interval [56]:

$$\mathbf{v_d^f} = \langle \mathbf{v} \rangle , \tag{26}$$

$$\mathbf{D^f} = \langle \mathbf{rv} \rangle - \langle \mathbf{r} \rangle \langle \mathbf{v} \rangle . \tag{27}$$

The bulk drift velocity $\mathbf{v_d^b}$ and diffusion coefficient $\mathbf{D^b}$ are defined relatively to the position of the *swarm center-of-mass* [19,57],

$$\mathbf{v_d^b} = \frac{d}{dt} \langle \mathbf{r} \rangle , \tag{28}$$

$$\mathbf{D^b} = \frac{1}{2} \frac{d}{dt} \langle (\mathbf{r} - \langle \mathbf{r} \rangle)^2 \rangle , \tag{29}$$

and are obtained from linear regressions to the swarm mean position $\langle \mathbf{r} \rangle$ and mean squared width $\langle (\mathbf{r} - \langle \mathbf{r} \rangle)^2 \rangle$, respectively (see Fig. 3).

Additionally, we calculate both bulk and flux components of the following swarm parameters:

- electron mobility - $\mu_e = v_{d,z}/E$;
- reduced Townsend coefficient - $\alpha_{ion}/N = k_{ion}/v_{d,z}$;
- reduced attachment coefficient - $\alpha_{att}/N = k_{att}/v_{d,z}$;
- characteristic energy - $\epsilon_{char} = D_\perp/\mu_e$, with $D_\perp = (D_x + D_y)/2$.

2.6.4. Power balance

The electron power-balance is analyzed by evaluating the kinetic energy changes in the ensemble of N_e electrons due to electric-field acceleration and collisions during the integration interval.

In the case of the electric-field acceleration, the energy change of one electron is simply $\Delta \epsilon_E^\mathcal{F} = \epsilon_a^\mathcal{F} - \epsilon_b^\mathcal{F}$, where $\epsilon_b^\mathcal{F}$ and $\epsilon_a^\mathcal{F}$ are the energies of the electron before and after the free-flight $\mathcal{F}$. Therefore, the total energy change of the electron ensemble during the integration interval is

$$\Delta E_E = \sum_{\text{all free-flights } \mathcal{F}} \epsilon_a^\mathcal{F} - \epsilon_b^\mathcal{F} . \tag{30}$$

To calculate the power gained/lost due to a collision kind $\mathcal{K}$, we must distinguish between conservative and non-conservative processes. For conservative processes, with no change in the number of electrons, the procedure is equivalent to the electric-field case:

$$\Delta E_{\text{coll},\mathcal{K}} = \sum_{\text{all coll. } c \text{ of kind } \mathcal{K}} \epsilon_a^c - \epsilon_b^c . \tag{31}$$

If the collision type $\mathcal{K}$ is an attachment, we subtract the energies of the incident electrons ϵ_b^c:

$$\Delta E_{\text{coll,att}} = \sum_{\text{all att. coll. } c} -\epsilon_b^c \,. \tag{32}$$

However, as we copy a random electron to keep N_e constant, we include an additional *electron energy growth term* [16]:

$$\Delta E_{\text{growth}}^{\text{att}} = \sum_{\text{all att. coll. } c} +\epsilon_r^c \,, \tag{33}$$

where ϵ_r^c is the energy of the copied electron. Concerning ionization, there is a loss of the ionization potential $\Delta\epsilon_{\text{ion}}$ for each collision event:

$$\Delta E_{\text{coll,ion}} = \sum_{\text{all ion. coll. } c} -\Delta\epsilon_{\text{ion}} \,. \tag{34}$$

Moreover, we include a growth contribution regarding the elimination of randomly-chosen electrons in ionization events:

$$\Delta E_{\text{growth}}^{\text{ion}} = \sum_{\text{all ion. coll. } c} -\epsilon_r^c \,, \tag{35}$$

where ϵ_r^c is the energy of the random electron removed after the ionization c.

The energy changes of the different processes ζ are converted into electron power-densities (per electron at unit gas density) as follows:

$$\frac{P_\zeta}{N} = \frac{1}{t - t_{ss}} \frac{\Delta E_\zeta}{N N_e} \,, \tag{36}$$

where N is the total gas density. As the sampling occurs only after the steady-state, the sum of the power densities should be null apart from statistical fluctuations:

$$\frac{P_E}{N} + \frac{P_{\text{coll}}}{N} + \frac{P_{\text{growth}}}{N} \simeq 0 \,. \tag{37}$$

Besides, by separating the terms above in gain and loss components, we can estimate the power-balance error using $\frac{\sum_\zeta (P/N)_{\text{gain},\zeta} + (P/N)_{\text{loss},\zeta}}{\sum_\zeta (P/N)_{\text{gain},\zeta}}$. This parameter provides an alternative way to quantify the statistical significance of the simulation.

2.7. Stopping criteria

The Monte Carlo simulation is stopped when the quality of the results fulfills the stipulated conditions. In LoKI-MC, there are various types of stopping criteria:

- minimum number of integration points;
- minimum number of real collisions per electron after reaching the steady-state;
- maximum tolerances for the relative standard deviations of the mean energy, flux drift velocity, flux diffusion coefficients and power balance;
- integration time-period, given as multiples of the steady-state time.

At least one of these criteria must be defined. The simulation is stopped when one of them is achieved. For the common user, the first criterion is more suited, since the appropriate values for the others may vary a lot with the gas and with E/N.

3. The LoKI-MC code

LoKI-MC is a Monte Carlo simulation tool that solves the electron kinetics for low-temperature plasmas excited by homogeneous DC electric fields in *any* complex gas mixture. The first release of the code assumes isotropic scattering in conservative collisions and an unbounded environment. Future releases will relax these two assumptions and will enable to study systems subject to a time-dependent electric field and/or a DC magnetic field. In this section, we present the input data necessary to run the code, focusing on its high flexibility, and we summarize the physical information given on the output.

3.1. Input

LoKI-MC solves the electron kinetics given: the physical working conditions (reduced field E/N, gas pressure p, gas temperature T_g and the gas-mixture composition); the distributions of populations ξ_{k_i}, $\xi_{k_{i_v}}$, $\xi_{k_{i_v J}}$ of electronic levels k_i, vibrational levels k_{i_v} and rotational levels $k_{i_v J}$, respectively (if applicable); and the sets of cross sections $\sigma_{k,c}^{\text{el}}$ (or $\sigma_{k,c}^{\text{eff}}$, see section 2.1), $\sigma_{k_{(i,j)}}$, $\sigma_{k_i,\text{att}}$ and $\sigma_{k_i,\text{ion}}$, where here i, j stand for any level of any gas k in the system.

Input parameters are set from a text input-file, in a user-friendly flexible way, e.g. allowing to (i) prepare simulations for either a sole value or a range of values of the applied reduced electric field; (ii) choose among different ionization models (SDCS/equal-sharing/no-sharing and isotropic/momentum-conservation scattering, see section 2.5); (iii) define the distributions of populations directly in the input file, from user-defined text files, or via functions for typical distributions at user-defined temperatures (e.g. Boltzmann or Treanor); (iv) list the filename(s) with the set(s) of cross sections to adopt in the simulations; (v) provide details about the numerical solution; (vi) select the output information (see next section). The code uses SI units for all physical quantities, except the energies, that are expressed in eV (electron-volt), and the reduced fields, that are expressed in Td (Townsend; 1 Td = 10^{-21} V m^2).

LoKI-MC uses electron scattering cross sections from the LXCat open-access website [23]. As input, the code accepts also *extra* sets of cross sections, which are not used in the calculation of the EEDF, but remain available for integration over the calculated EEDF, to obtain rate coefficients with interest for various purposes (e.g. global models, spectroscopy analysis, actinometry diagnostics, etc.). For more details on the format of the LXCat files used in the code, see the section 3.3 of the LoKI-B paper [16].

The numerical conditions are set by defining: (i) the number of electrons in the ensemble; (ii) inclusion (or not) of a thermal motion for the neutral gas; (iii) criteria for finishing the simulation. Additionally, it is possible to set the numbers of cells used in the discretization of the distribution functions (see section 2.6.1) and the number of grid points used to linearly interpolate the cross sections (by default, 10^4). The maximum energy of the cross-section grid is defined dynamically during the simulation. If, at any point of the simulation, this value is higher than the maximum energy of one elastic cross section, the code stops and throws an error.

3.2. Output

The simulation tool provides as output: (i) the EEDF f_0 and the anisotropies f_1 and f_2; (ii) the EVDF $f(v_r, v_z)$; (iii) bulk and flux swarm parameters together with statistical errors; (iv) collision rate-coefficients, including the *extra* ones; (v) power balance; (vi) spatiotemporal evolution of the electron swarm (mean values of the energy, position, velocity and squared-width, as a function of time); (vii) details of the Monte Carlo simulation (e.g. number of electron collisions before and after the steady-state). If the graphical interface is activated, most of this information can be plotted in the end of the simulation, allowing the user to check immediately the quality of the results.

Table 1

Comparison of LoKI-MC solutions with MultiBolt calculations [18] and previous MC results [51,57], for the Reid-ramp model [45]. The standard deviations σ [%] of the LoKI-MC simulations are shown in squared parenthesis. The deviations δ between LoKI-MC results (LMC) and previous results (PR), defined as δ [%] $= (1 - \text{PR}/\text{LMC}) \times 100$, are shown in curved parenthesis.

|		$\langle\epsilon\rangle$ (eV)	v_d^b (10^4 m s^{-1})	$D_T^b N$ (10^{24} m^{-1} s^{-1})	$D_L^b N$ (10^{24} m^{-1} s^{-1})
$E/N = 1$ Td	LoKI-MC	0.1014 [0.06]	1.264 [0.43]	0.9637 [0.70]	0.7542 [0.68]
	MultiBolt [18]	0.1014 (0.00)	1.272 (-0.63)	0.9746 (-1.13)	0.7593 (-0.68)
	MCC [51]	0.1017 (-0.30)	1.273 (-0.71)	0.966 (-0.24)	0.7575 (-0.44)
	MCC [57]	0.1015 (-0.10)	1.271 (-0.55)	0.974 (-1.07)	0.757 (-0.37)
$E/N = 12$ Td	LoKI-MC	0.2691 [0.10]	6.838 [0.09]	1.137 [0.44]	0.5679 [0.35]
	MultiBolt [18]	0.2688 (0.11)	6.839 (-0.01)	1.134 (0.26)	0.5688 (-0.16)
	MCC [51]	0.2703 (-0.45)	6.834 (0.06)	1.140 (-0.26)	0.569 (-2.41)
	MCC [57]	0.2693 (-0.07)	6.833 (0.07)	1.136 (0.09)	0.5816 (-2.41)
$E/N = 24$ Td	LoKI-MC	0.4081 [0.10]	8.881 [0.07]	1.138 [0.53]	0.4595 [0.56]
	MultiBolt [18]	0.40922 (-0.27)	8.8522 (0.32)	1.137 (0.09)	0.4601 (-0.13)
	MCC [51]	0.4113 (-0.78)	8.804 (0.87)	1.131 (0.62)	0.4546 (1.07)
	MCC [57]	0.4085 (-0.10)	8.878 (0.03)	1.140 (-0.18)	0.4684 (-1.94)
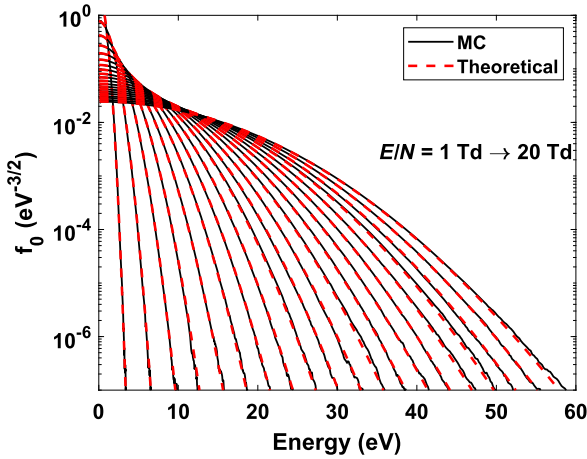
Fig. 4. Electron energy distribution functions obtained in LoKI-MC using the Druyvesteyn model for E/N values from 1 to 20 Td.

4. Results

This section provides a comprehensive set of results obtained with LoKI-MC for different gases. First, the formulation is verified in well-established model gases, comparing it against analytical solutions and other published works. Then, the code is benchmarked against the two-term solver LoKI-B and the ten-term solver MultiBolt using the real gases O_2 and Ar. Finally, the effects of anisotropic ionization scattering and superelastic collisions, which are neither considered in MultiBolt nor in METHES, are analyzed in real gases. The examples were chosen so as to highlight the reliability and flexibility of the present code. In all simulations, we keep the default values for the numbers of cells used to discretize the distribution functions and for the number of grid points to interpolate the cross sections (cf. section 2).

4.1. Verifications in model gases

For the model gases, we use an ensemble of 10^5 electrons. The simulations are stopped when the following requirements for the maximum standard deviations are met: mean energy (0.1%), flux drift velocity (0.4%), flux diffusion coefficients (0.8%) and power balance (0.01%).

We start by analyzing a simple model where scattering events are restricted to elastic collisions with the gas molecules ($M = 4$ amu), characterized by a constant elastic momentum-transfer cross-section $\sigma_c^{\text{el}} = 6 \times 10^{-20}$ m^2. In this case, the system can be described analytically and the Druyvesteyn distribution is obtained

at steady-state [58]. Since the model assumes the neutrals at rest, the thermal motion of the molecules is deactivated in these simulations. In Fig. 4, the EEDFs from Monte Carlo simulations are compared with the analytical Druyvesteyn solutions for reduced electric fields from 1 to 20 Td, revealing a remarkable agreement over at least five orders of magnitude.

In the next verification, we add to the previous model a linearly increasing excitation cross-section $\sigma_c^{\text{ex}} = (\epsilon - 0.2) \times 10^{-19}$ m^2, with energy threshold of 0.2 eV, obtaining the well-known Reid-ramp model [45]. Three values of E/N are used: 1, 12 and 24 Td. LoKI-MC simulations are compared with MultiBolt [18] and the Monte Carlo results of Raspopović et al. [51] and White et al. [57], as shown in Table 1. There is an excellent agreement with the results obtained by other codes, for all parameters.

To verify LoKI-MC in the presence of non-conservative collisions, both *ionization* and *attachment*, the non-conservative model gas of Lucas-Saelee [59] was employed, along with the attachment modifications of Ness and Robson [60]. The results are not shown here and the detailed comparison with previous works [18,51,53] can be found in the documentation of the code. The agreement is very good, exhibiting differences within two standard deviations.

Another important verification consists on analyzing the swarm behavior in zero-field conditions, in order to assess the validity of the treatment of low energy electron-molecule collisions. In this case, the electron swam should relax towards a Maxwellian distribution at the background gas temperature (T_g), independently of the initial condition. To test this behavior, we use the Druyvesteyn model, but now including the influence of the thermal motion of the molecules. Fig. 5 presents the temporal evolution of the swarm energy for three initial electron temperatures ($0.5 T_g$, T_g, $1.5 T_g$, with $T_g = 300$ K) at $E/N = 0$ Td. As expected, the swarm energy tends to the gas mean energy, $\frac{3}{2} k_B T_g$, independently of the initial conditions. Note also that, if we do not consider the gas-temperature effect in the collision dynamics, the electron swarm tends to zero energy, which stresses the importance of the correct treatment of electron-molecule collisions at low E/N. Finally, Fig. 6 shows that, in zero-field conditions, the EEDF from Monte Carlo simulations is in fact a Maxwellian at the temperature of the background gas.

4.2. Benchmark in real gases

For the benchmark in real gases, we use an ensemble of 5×10^4 electrons in all simulations, except in the case of the bulk diffusion coefficients and characteristic energy, where we use 5×10^5 electrons for $E/N \geq 100$ Td to overcome the statistical fluctuations associated with secondary electrons in ionization. The simulations are stopped after 10^5 integration points. The gas temperature is
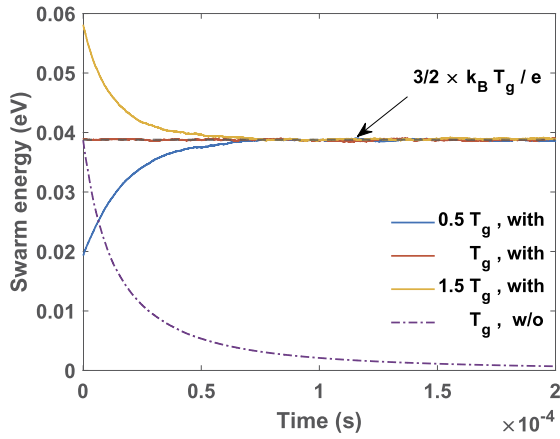
Fig. 5. Temporal evolution of the swarm energy in zero-field conditions for three initial electron temperatures ($0.5T_g$, T_g, $1.5T_g$, with $T_g = 300$ K), with and without the gas-temperature effect.
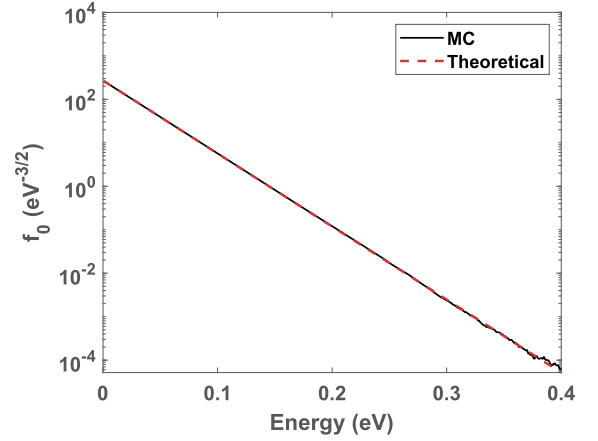

Fig. 6. Comparison of the steady-state EEDF, in zero-field conditions, with the theoretical Maxwellian at 300 K.
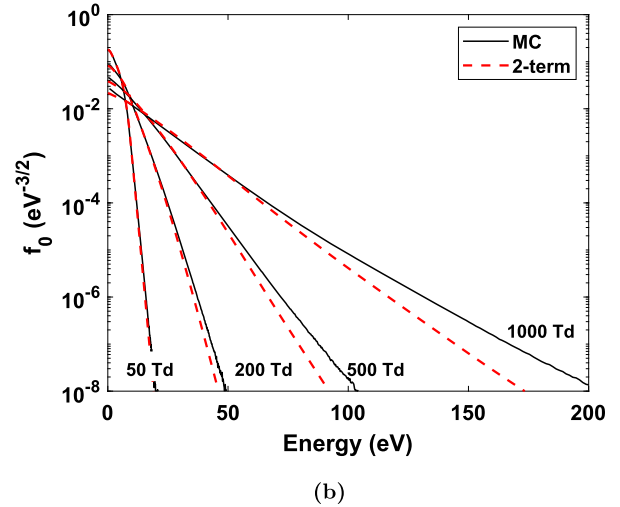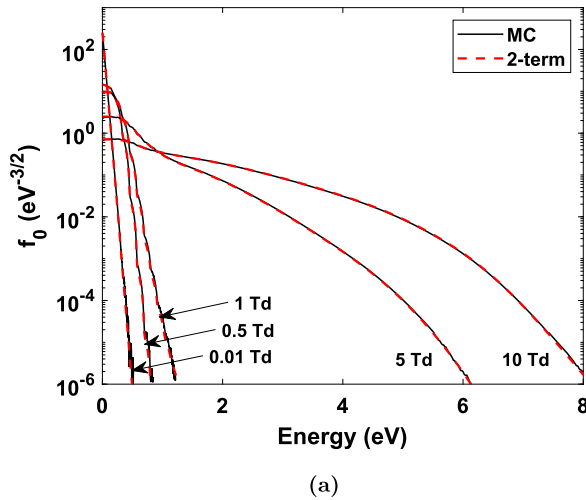

(a)

(b)

Fig. 7. Electron energy distribution functions in oxygen obtained with LoKI-MC and LoKI-B (two-term solver), for various reduced electric fields: (a) 0.01 - 10 Td; (b) 50 - 1000 Td.

300 K and isotropic ionization scattering is considered. We start by presenting the results in molecular oxygen, comparing the present simulations with the two-term solver LoKI-B. Then, we compare the results in atomic argon obtained with both LoKI-B and Multi-Bolt.

4.2.1. Molecular gas: oxygen

In molecular oxygen, the simulations are performed for reduced electric fields from 0.005 to 1000 Td and the energy sharing in ionization is described by a SDCS [47]. LoKI-B simulations are done in an energy grid with 1000 cells and dynamical maximum energy value, ensuring a decay of 12 decades in the EEDF and a power-balance error of 10^{-9}. LoKI-B and LoKI-MC simulations use data published in the IST-Lisbon database of LXCat [61], namely the O_2 complete set of electron-scattering cross sections, complemented by the O_2-rot dataset for the description of rotational transitions. For details on these cross sections, see section 4.4 of the LoKI-B paper [16].

In Fig. 7, the EEDFs are presented for several values of the reduced field. Until 50 Td, the agreement between LoKI-MC and LoKI-B is remarkable. For $E/N \gtrsim 200$ Td, the anisotropies start to be significant, thereby leading to visible deviations from the two-term calculations.

Fig. 8 shows various electron swarm parameters in oxygen as a function of E/N. As expected, the flux component of the mobility coincides with the LoKI-B results. For ~ 200 Td, the bulk mobility starts to deviate from the flux component due to the significant contribution of secondary electrons in ionization. The agreement in the transverse diffusion coefficient is poor for $E/N \gtrsim 50$ Td. This inaccuracy of the diffusion coefficients calculated by means of the two-term approximation is well known [19,26]. The same splitting between flux and bulk components is observed for the diffusion coefficient. The flux characteristic energy and the electron temperature from LoKI-MC are in accordance with LoKI-B, and for low electric fields both parameters tend to the corresponding values at 300 K gas temperature, as expected. The deviations for $E/N > 100$ Td in the flux characteristic energy are related to the transverse diffusion coefficient. Finally, the Townsend ionization and attachment coefficients reveal a good agreement between the MC and 2-term calculations. The normalized electron power-transfer in oxygen is detailed in Fig. 9. The electron energy gain is controlled by rotational superelastic collisions for reduced fields $E/N \lesssim 0.5$ Td and by the electric field for higher E/N. The electron energy loss is driven mainly by rotational excitation for $E/N \lesssim 0.5$ Td, followed by vibrational excitation until $E/N \lesssim 10$ Td, and by electronic and ionization collisions for higher E/N. Note that the contribution of the secondary electrons
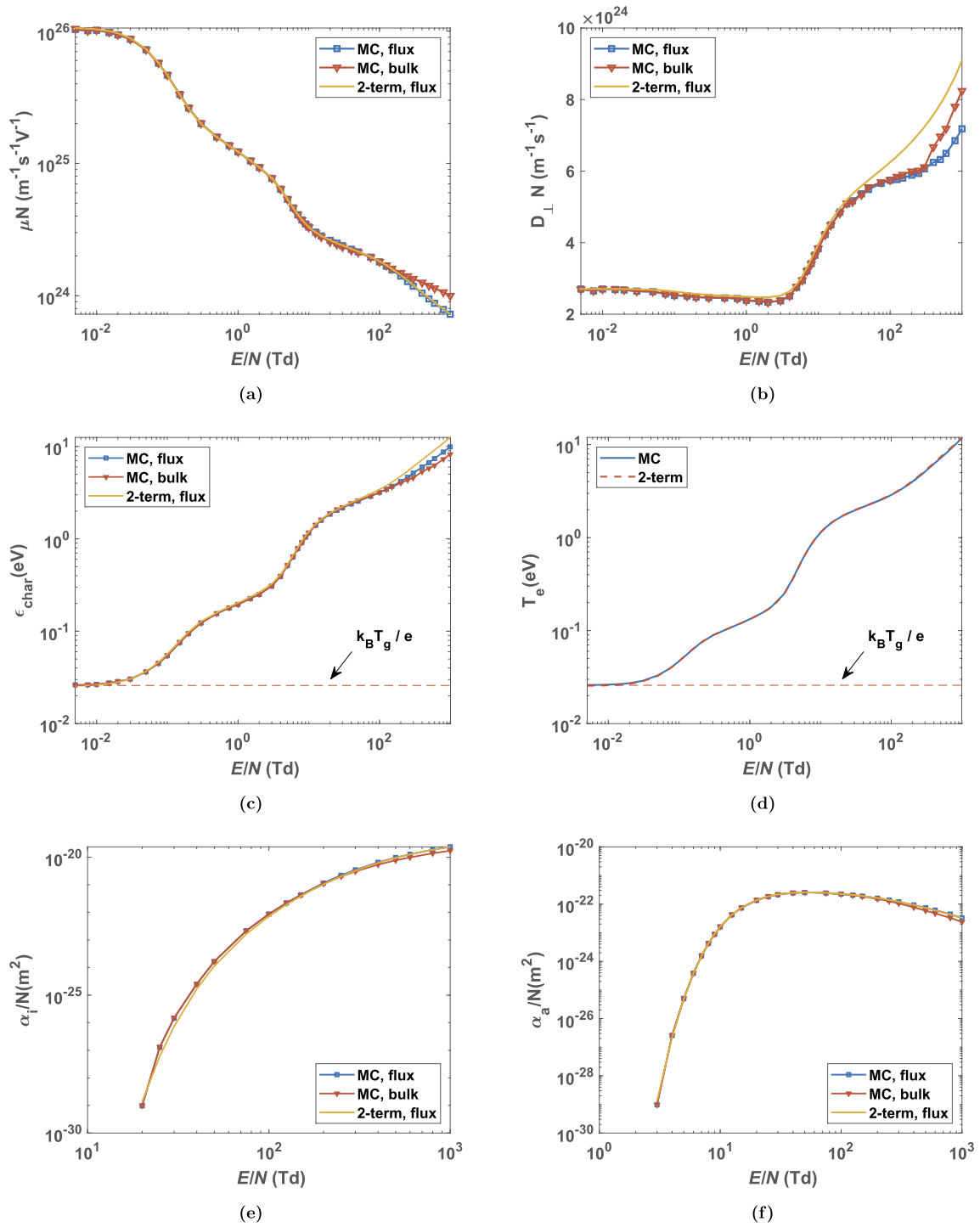
Fig. 8. Electron swarm parameters in molecular oxygen ($T_g = 300$ K) as a function of E/N, obtained with LoKI-MC and LoKI-B (2-term solver): (a) reduced mobility; (b) reduced transverse diffusion coefficient; (c) characteristic energy; (d) temperature; (e) Townsend ionization coefficient; (f) Townsend attachment coefficient.

in ionization, accounted in the electron growth term, is very important above 200 Td. The significant influence of rotations and vibrations in the electron power balance reinforces the idea that a detailed description of the internal states of the molecules is essential to obtain accurate results in a wide range of conditions, specially if the associated temperatures are high, as discussed in section 4.5.

4.2.2. Atomic gas: argon

The simulations in argon are performed for reduced electric fields from 1 to 1000 Td, considering equal-energy sharing in ion-

ization, to allow for a direct comparison with MultiBolt. MultiBolt was run with a ten-term expansion in Legendre polynomials in hydrodynamic regime [18], using 1000 energy points and ensuring a convergence error of 5×10^{-6} for the electron mean energy. The numerical parameters in LoKI-B are the same as in the previous section. All calculations use the `Ar` complete set of cross sections, published in the IST-Lisbon database of LXCat [62].

The EEDFs in argon are shown in Fig. 10. For E/N below 50 Td, the agreement between the three solvers is remarkable. For higher fields, the two-term solutions diverge from the Monte Carlo
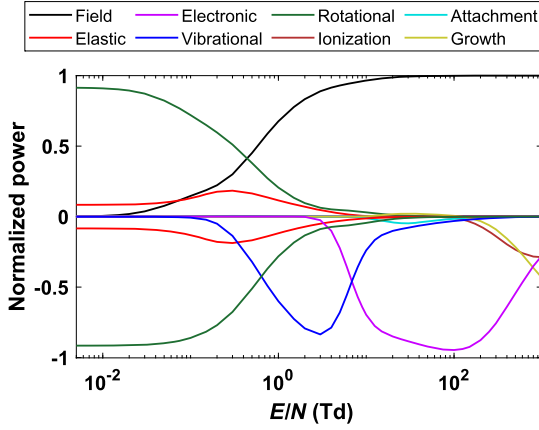
Fig. 9. Normalized electron power transferred to various gain (positive values) / loss (negative) channels in oxygen, as a function of the reduced electric field. (For interpretation of the colors in the figure(s), the reader is referred to the web version of this article.)

and the multi-term results, due to the breakdown of the low-anisotropy condition, while the latter two preserve the good agreement.

The electron swarm parameters in argon are presented in Fig. 11. The flux contribution of the mobility reveals an excellent agreement between the three approaches, except for a small difference in the LoKI-MC results at 1000 Td. Both LoKI-MC and MultiBolt predict the same splitting in the trends of the bulk and the flux components of the mobility, above ~ 50 Td. The transverse diffusion coefficient from LoKI-MC agrees well with those predicted by MultiBolt, for the range of E/N considered, while the two-term values are significantly shifted. As expected, this difference affects also the characteristic energy calculated with the two-term code. There is good agreement between the predictions of the three codes for the electron temperature and the Townsend coefficients. Finally the LoKI-MC and MultiBolt results for the longitudinal diffusion coefficient differ for $E/N \gtrsim 300$ Td, which is probably caused by the breakdown of the second-order expansion used in Multibolt to calculate the diffusion and mobility coefficients [18].

4.3. Anisotropies

In the last sections, we have confirmed that the two-term approximation fails for sufficiently high reduced electric fields (and

possibly in other conditions, depending on the gas), as discussed in the literature [24–27]. We can gain insight into the underlying reasons for this limitation by analyzing the EVDFs. Fig. 12 shows the EVDFs in molecular oxygen obtained for two E/N values. At 10 Td, the center of the EVDF is still close to the origin, exhibiting various "striations" caused by vibrational and electronic transitions. At 500 Td, the large electric field visibly shifts the entire distribution towards the forward z-direction. Since the two-term approximation lies on a nearly isotropic EVDF with small deviations around the axial direction, this is clearly not valid at 500 Td. Fig. 13 presents the ratio of the lower-order anisotropies, averaged over all energies, $\frac{\langle |f_{1,2}| \rangle}{\langle f_0 \rangle} \equiv \int_0^\infty |f_{1,2}(\epsilon)| d\epsilon / \int_0^\infty f_0(\epsilon) d\epsilon$, calculated with LoKI-MC in oxygen and argon. In molecular oxygen, the anisotropies increase in the regions where the rotations and vibrations are relevant. Moreover, in both gases, there is a continuous increase of the ratios with the reduced electric field. Taking $\frac{\langle f_1 \rangle}{\langle f_0 \rangle} \lesssim 0.2$ as a criterion for the validity of the two-term approximation, one concludes that this condition breaks for $E/N \gtrsim 50$ Td in the case of oxygen and for $E/N \gtrsim 200$ Td in the case of argon. For example, in typical nanosecond discharges, where the reduced field may reach several hundreds of Td [31,32], the two-term approximation can lead to faulty results.

4.4. Anisotropic ionization scattering induced by momentum conservation

In the previous sections, we considered isotropic scattering in ionization collisions for both scattered and secondary electrons, since this assumption is used in the Boltzmann solvers LoKI-B and MultiBolt. However, as discussed in section 2.5, this approach does not conserve the linear momentum in the collision and, if possible, should be avoided. Here, the influence of anisotropic scattering in ionization collisions, induced by momentum conservation, is analyzed in argon. Fig. 14 shows that at 500 Td the EEDFs with/without anisotropic scattering are still similar, while for 800 and 1000 Td the tails of the distributions are clearly higher when using an anisotropic description. As shown in Fig. 15, this effect is also noticed in the mobility and the diffusion coefficients, where the parameters are significantly higher when anisotropic scattering is considered for reduced fields $E/N \gtrsim 200$ Td (deviations up to 14%, 15%, 17% and 40%, for the flux mobility, bulk mobility, flux transverse diffusion and flux longitudinal diffusion coefficients, respectively). The previous observations do not imply that anisotropic scattering should be adopted in all cases, since
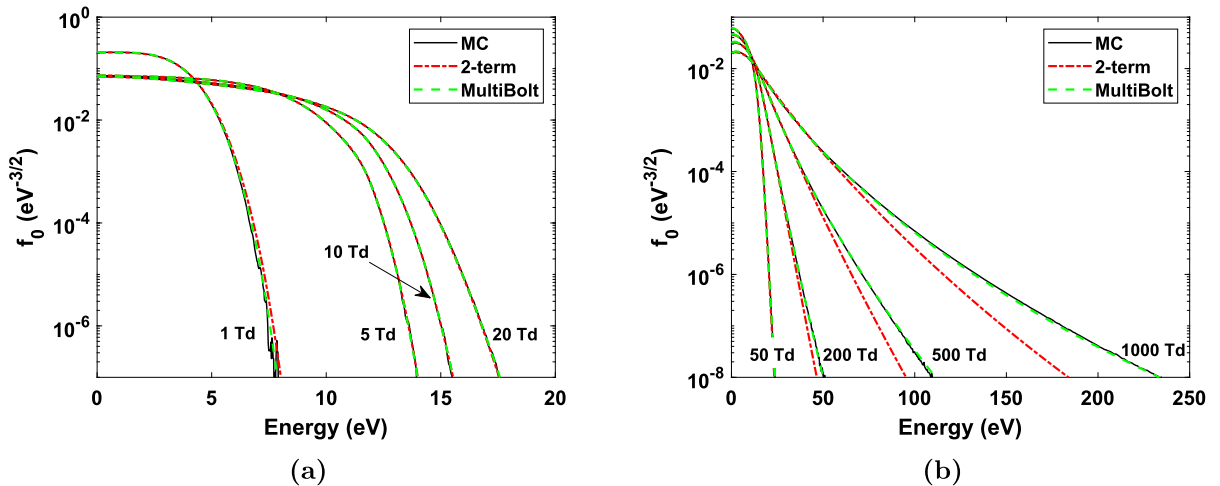

Fig. 10. Electron energy distribution functions in argon, obtained with LoKI-MC, LoKI-B (2-term solver) and MultiBolt (10-term solver) for various reduced electric fields: (a) 1-20 Td; (b) 50-1000 Td.
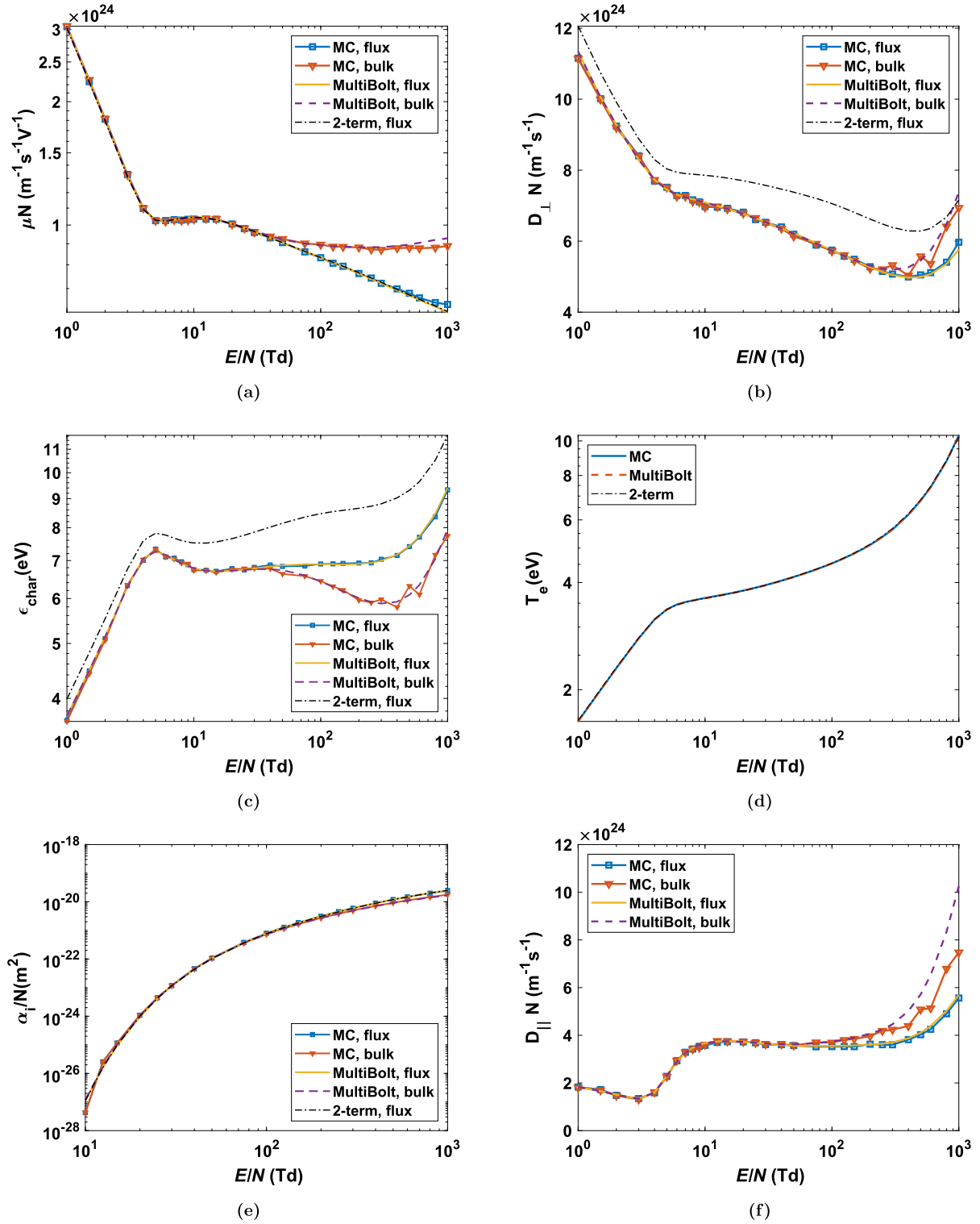
Fig. 11. Electron swarm parameters in argon ($T_g = 300$ K) as a function of E/N, obtained with LoKI-MC, LoKI-B (2-term solver) and MultiBolt (10-term solver): (a) reduced mobility; (b) reduced transverse diffusion coefficient; (c) characteristic energy; (d) temperature; (e) Townsend ionization coefficient; (f) reduced longitudinal diffusion coefficient.
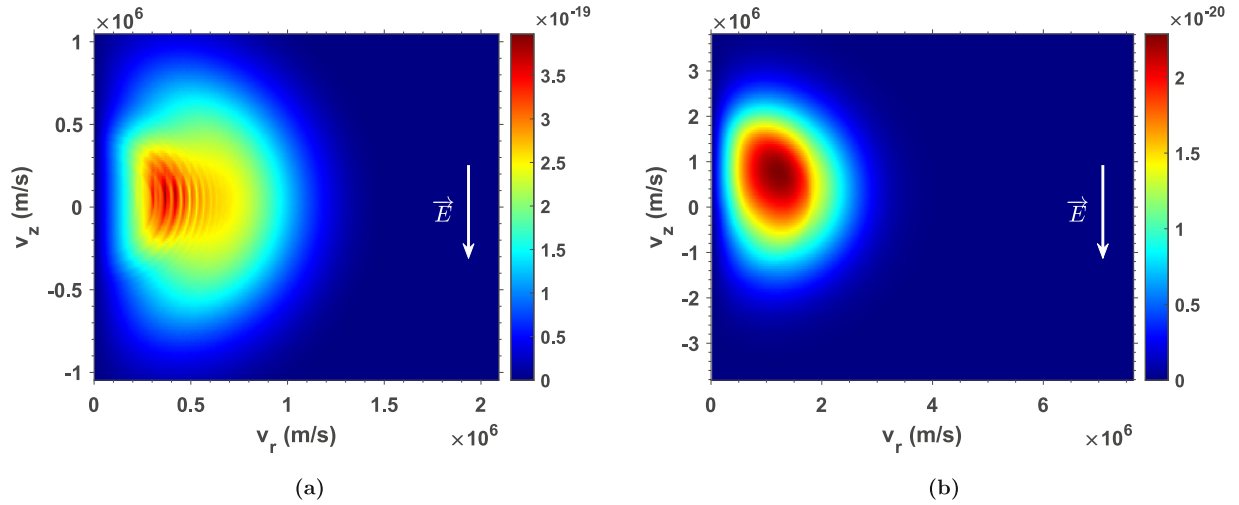
Fig. 12. Electron velocity distribution function ($m^{-3}\,s^3$) in molecular oxygen for the following E/N values: (a) 10 Td; (b) 500 Td.
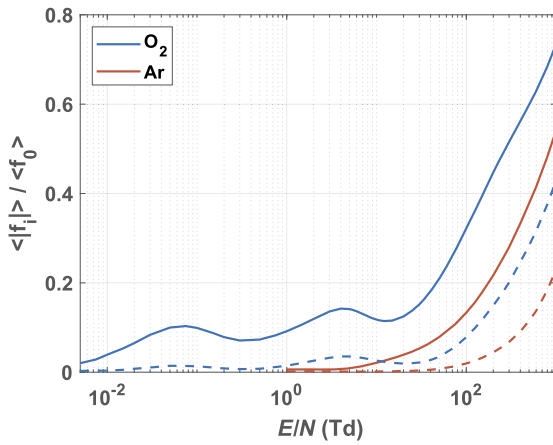
Fig. 13. Average anisotropy ratios in oxygen and argon, as a function of E/N: $\frac{\langle |f_1| \rangle}{\langle f_0 \rangle}$ (full lines); $\frac{\langle |f_2| \rangle}{\langle f_0 \rangle}$ (dashed).
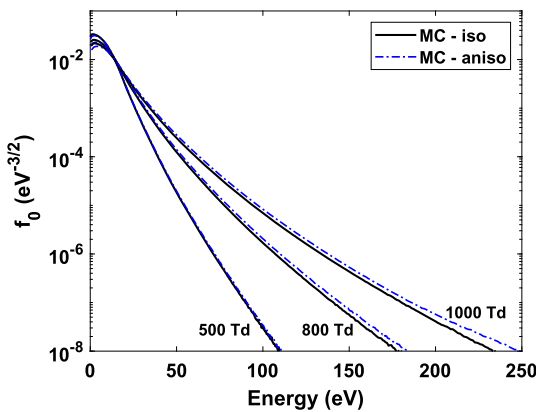

Fig. 14. Electron energy distribution functions in argon using isotropic and anisotropic scattering in ionization events, at various E/N values.

most cross-section sets were optimized assuming isotropic scattering in ionization events. Therefore, the use of anisotropic scattering, while physically more correct, may lead to a worst comparison with the measurements of swarm parameters, depending on the cross-section data used.

4.5. Effects of superelastic collisions

This section analyzes the effects of superelastic collisions in two systems, using a typical reduced electric field of 50 Td, so as to demonstrate the importance of a detailed description of the internal states of the gas. Molecular oxygen and molecular nitrogen are used to illustrate the influence on the electron kinetics of electronically and vibrationally excited states, respectively.

The first electronically excited state of molecular oxygen, $O_2(a^1\Delta_g)$, is significantly present in typical discharge conditions, with fractional populations of the order of 0.15 [63–67]. The EEDFs in molecular oxygen are shown in Fig. 16 for different $[O_2(a)]/N$ fractions. We find that the larger the excited $O_2(a)$ population, the higher is the tail of the distribution, as expected, due to the increasing influence of the electron superelastic collisions with this excited state [63]. The differences at high energies may have a significant impact when coupling the results of the electron kinetics to the heavy-species chemistry. For example, the ionization rate coefficient, in units of 10^{-19} m^3/s, is 1.77, 3.03 and 5.18, for $[O_2(a)]/N$ fractions of 0, 0.1 and 0.2, respectively. Therefore, the modeling of oxygen discharges with relative $O_2(a)$ populations as low as 0.1 should not be based on the ground-state approximation.

It is well known that the vibrationally excited states of nitrogen strongly influence the electron kinetics [29,68–71]. To illustrate this effect, we use the N_2 complete set of cross sections, together with the N_2-vib cross sections describing the vibrational electron-molecule collisions, published in the IST-Lisbon database of LXCat [72]. The latter set of cross sections describes all vibrational excitations/de-excitations between the first 11 levels of the ground state. For more details on the N_2 cross-section set, see section 4.3 of [16]. The energies of the vibrational levels are set according to the energy thresholds of the cross sections for vibrational excitation.[1] The EEDFs in nitrogen are presented in Fig. 17, considering Maxwell-Boltzmann vibrational distribution functions at three temperatures, $T_v = 300, 2000, 5000$ K. The results show that the EEDFs strongly change with the vibrational temperature, exhibiting an enhanced plateau above 2 eV as T_v increases, due to the effects of vibrational de-excitation and the associated transfer of energy to the electrons. These changes affect significantly the electron rate coefficients. For example, the ionization rate coefficient, in units of 10^{-22} m^3/s, is 2.25, 4.51 and 24.7, for vibrational

---

[1] We checked that in conditions of null electric field and temperature of 2000 K, where thermalization is significantly influenced by the vibrational distribution, the EEDF tends to a Maxwellian at the corresponding temperature, as expected.
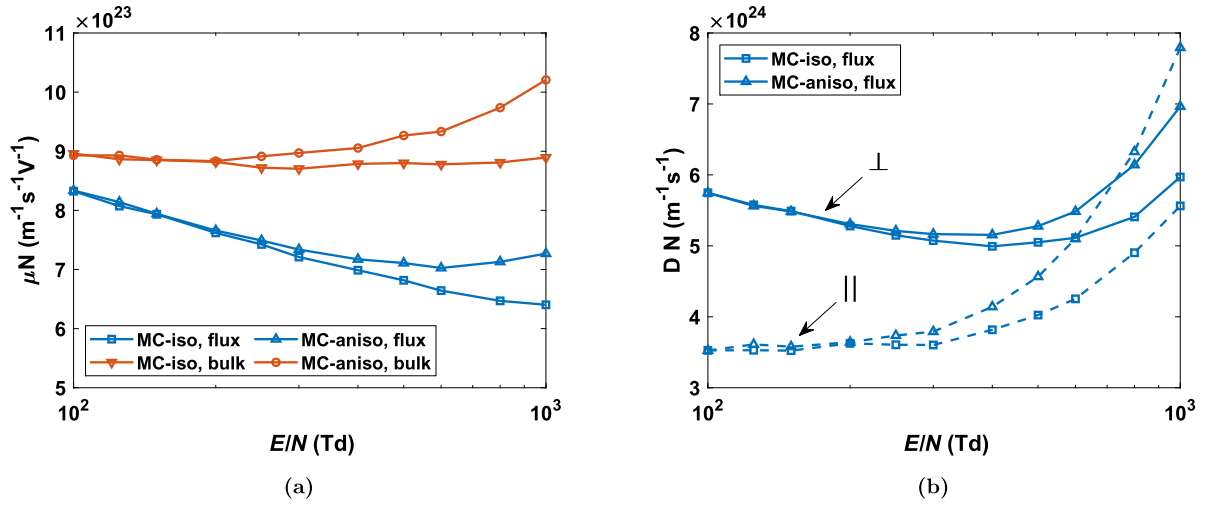
Fig. 15. Swarm parameters in argon, as a function of E/N, using isotropic and anisotropic scattering in ionization events: (a) reduced mobility; (b) reduced transverse (full lines) and longitudinal (dashed) flux diffusion coefficients.
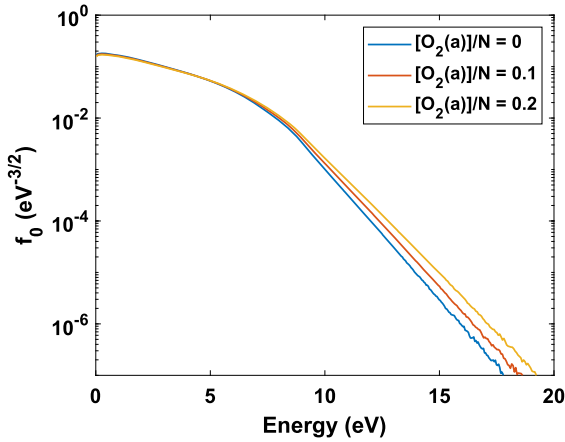

Fig. 16. Electron energy distribution functions in oxygen at $E/N = 50$ Td, for different fractions $[O_2(a)]/N$.
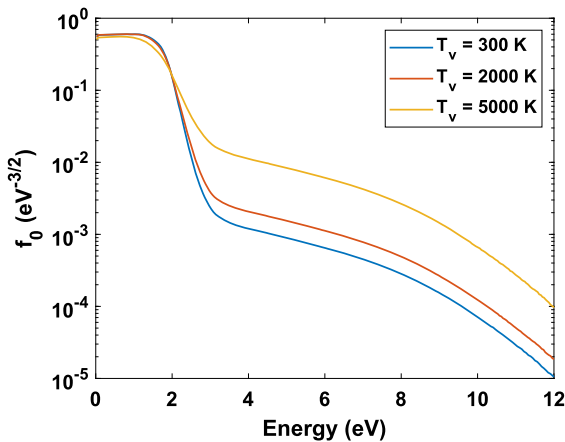

Fig. 17. Electron energy distribution functions in nitrogen at $E/N = 50$ Td, for different vibrational temperatures T_v.

temperatures of 300, 2000 and 5000 K, respectively. Considering that the vibrational temperatures in N_2 discharges can reach 10000 K, the electron kinetics should be described taking into account the vibrational distribution function.

4.6. Computation time

The major drawback of Monte Carlo simulations is the long computation time. However, due to the continuous advancing on computing efficiency, using Monte Carlo codes is becoming affordable. Furthermore, LoKI-MC is relatively fast. Fig. 18 compares the computation times of LoKI-MC and METHES [19], using an ensemble of 10^4 electrons in argon at $E/N = 500$ Td. Both codes are run using one thread of a dual-core processor Intel(R) Core(TM) i7-6500U @ 2.50 GHz, considering for LoKI-MC three different options for the gas-temperature effect: false (not considering this effect), true (activating this effect) and smart activation (considering the thermal motion of the molecules only when the electron energy is relatively low, see section 2.4). In all cases, the computation time of LoKI-MC is remarkably shorter than of METHES. With the gas-temperature effect set to "false" or "smart activation", LoKI-MC is ~ 17 times faster than METHES to simulate 2×10^8 electron collisions, while with "true", it is ~ 9 times faster. The great disparity in the computational performance is due to a conjugation of two factors: for the type of calculations required in a MC code, C++ is much more efficient than MATLAB; METHES alters class objects several times, which is computationally expensive in MATLAB. Note that the LoKI-MC simulation with 2×10^8 collisions, using the "smart activation" option, takes around 2.3 min and already provides reasonable results, with relative standard deviations of 0.3%, 0.5% and 1.3% for the mean energy, the flux drift velocity and the flux diffusion coefficients, respectively.

If the simulations are run with two threads, the difference between the computation times of LoKI-MC and METHES is ~ 1.5 times larger than before, since LoKI-MC is partially parallelized, contrarily to METHES. The parallelization is performed using OpenMP [73] for handling free-flights, collision dynamics and generation of random numbers. More parallelization might happen outside of the LoKI-MC itself: the Eigen library [74] is used for matrix/vector data types and operations, and that can parallelize various operations itself, depending on the capabilities of the host architecture and on compiler flags that can be specified at build-time. For large problems, the usage of distributed methods (MPI) may be required in addition to the local parallelization implemented at this moment.

The speedup factor associated with the LoKI-MC parallelization is studied in a workstation with two processors Intel(R) Xeon(R) Platinum 8170 @ 2.10 GHz, each composed by 26 cores with hyperthreading. Using the same simulation conditions, the code is run with different number of threads: 1, 2, 4, 8, 16. The speedup
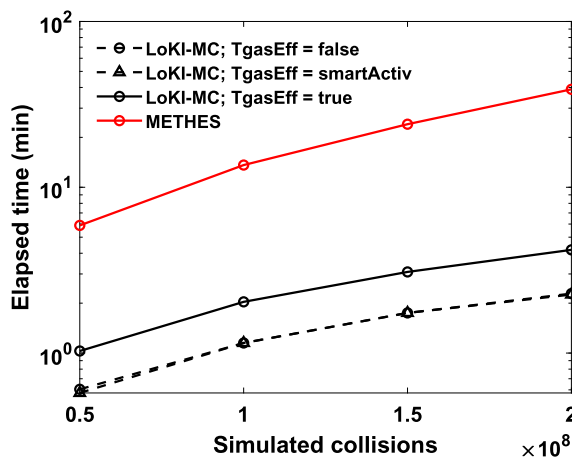
Fig. 18. Monte Carlo computation times using LoKI-MC and METHES [19] with 10^4 electrons, in argon at $E/N = 500$ Td, as a function of the number of simulated collisions.

Fig. 19. Comparison between the speedup factor of LoKI-MC, $S_{\mathrm{LoKI-MC}}$, and the theoretical Amdahl formula, $S_{\mathrm{th}}(\tau)$, presented in the text.

factor of LoKI-MC, $S_{\mathrm{LoKI-MC}}$, is presented in Fig. 19, as a function of the number of threads. The trend is compatible with the theoretical behavior of the Amdahl's law [75], typical in tasks with fixed size: $S_{\mathrm{th}}(\tau) = (1 - p + p/\tau)^{-1}$, where p is the proportion of the code that is parallelized and τ is the number of threads used in the tasks. As shown in Fig. 19, $S_{\mathrm{LoKI-MC}}$ agrees rather well with $S_{\mathrm{th}}(\tau)|_{p=0.64}$, which suggests that approximately 64% of the tasks are parallelized. Therefore, in principle, the speedup factor cannot be higher than $(1 - 0.64)^{-1} \simeq 2.78$. One may ask why the rest of the code is not parallelized. The calculations are parallelized along the ensemble of electrons. Most of the operations concerning free flights, collision choices and collision dynamics can be performed in parallel. However, part of the calculations rely on shared-memory reading, which may harm the parallelization efficiency. Moreover, there are some operations that cannot be fully parallelized: to obtain the swarm parameters at each time-instant, several sums and averages are done; after solving the collision dynamics of the ensemble, the collision and power-balance counters need to be updated.

Computation profiling, e.g. using Valgrind's callgrind [76], may help to understand and mitigate parallelization bottlenecks, and even to optimize the single-thread behavior. A preliminary analysis indicates that approximately 50% of the computation time is spent on the collision choice. Therefore, for future releases, we will focus on the optimization of this part of the code, in order to decrease as much as possible the computation time.

The simulations in real gases presented in section 4.2 (5×10^4 electrons and 10^5 integration points) take around 20 minutes per E/N value, using two threads of the dual-core processor mentioned previously. This is significantly larger than the computation times of LoKI-B (~ 1 s) and MultiBolt (~ 40 s). Nonetheless, the Monte Carlo LoKI-MC provides additional insight into the behavior of the plasma electron kinetics, since it provides the EVDF (instead of only some of its anisotropies), it allows including the thermal motion of the gas in the description of collisional events, and it accounts for the influence in the electron kinetics of the internal states of the neutral atoms / molecules.

5. Final remarks and future work

This paper presented LoKI-MC, a flexible and highly-performant open-source simulation tool, which uses Monte Carlo techniques to solve the non-equilibrium electron kinetics of plasmas excited by uniform DC electric fields. LoKI-MC simulates plasmas produced from any gas mixture, accounting for the distributions of popula-
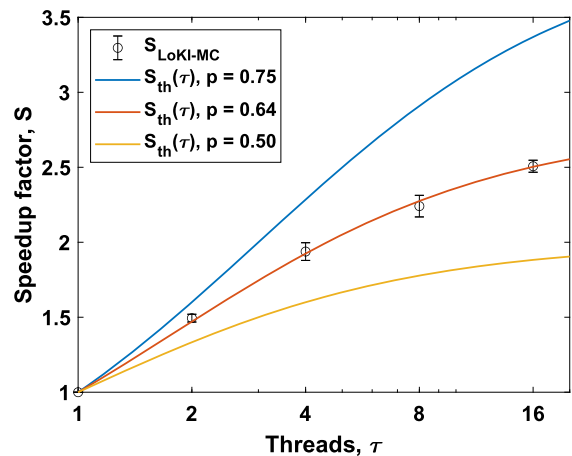
tions for the electronic, vibrational and rotational atomic/molecular levels. The output comprises the EEDF, the EVDF, the electron swarm parameters, the distribution of electron power transferred to the different collisional channels and the spatiotemporal evolution of the electron swarm. The simulation tool has been verified and benchmarked in model gases and real gases, through the comparison with analytical solutions, previous works and other simulation tools. Furthermore, the effects of the gas temperature, anisotropic ionization scattering (induced by momentum conservation) and superelastic collisions were assessed in real gases.

LoKI-MC is freely available for users to perform electron kinetics calculations. Moreover, modelers are invited to continue testing and/or improving the simulation tool. Due to the efficient nature of the C++ code, LoKI-MC can be embedded in plasma-chemistry or fluid models for the calculation of electron rate coefficients and transport parameters.

Future versions of LoKI-MC will include (i) the description of time-dependent electric fields, (ii) magnetic fields, (iii) anisotropic scattering defined by angle-resolved differential cross sections, for any collision type, (iv) charged-particle collisions and (v) the possibility of considering bounded environments. Furthermore, the algorithm presented here to study the electron kinetics will be adapted and coupled to the Kinetic Monte Carlo formulation presented in [28] to study the chemical kinetics, in order to obtain a self-consistent and unified description of plasma-chemistry, valid in any timescale and at any reduced electric field.

Declaration of competing interest

The authors declare that they have no known competing financial interests or personal relationships that could have appeared to influence the work reported in this paper.

Data availability

The data used for this article is published with the code.

Acknowledgements

References

[1] G.S. Oehrlein, S. Hamaguchi, Plasma Sources Sci. Technol. 27 (2) (2018) 023001.

[2] J.T. Gudmundsson, N. Brenning, D. Lundin, U. Helmersson, J. Vac. Sci. Technol. A 30 (3) (2012) 030801.

[3] C. Labay, I. Hamouda, F. Tampieri, M.-P. Ginebra, C. Canal, Sci. Rep. 9 (1) (2019) 16160.

[4] G. Bauer, D.B. Graves, Plasma Process. Polym. 13 (12) (2016) 1157–1178.

[5] G. Fridman, G. Friedman, A. Gutsol, A.B. Shekhter, V.N. Vasilets, A. Fridman, Plasma Process. Polym. 5 (6) (2008) 503–533.

[6] M. Gherardi, N. Puač, M. Shiratani, Plasma Process. Polym. 15 (2) (2018) 1877002.

[7] S.C. Min, S.H. Roh, B.A. Niemira, J.E. Sites, G. Boyd, A. Lacombe, Int. J. Food Microbiol. 237 (2016) 114–120.

[8] S. Kitazaki, K. Koga, M. Shiratani, N. Hayashi, Jpn. J. Appl. Phys. 51 (1) (2012) 01AE01.

[9] G.J. van Rooij, D.C.M. van den Bekerom, N. den Harder, T. Minea, G. Berden, W.A. Bongers, R. Engeln, M.F. Graswinckel, E. Zoethout, M.C.M. van de Sanden, Faraday Discuss. 183 (2015) 233–248.

[10] R. Snoeckx, R. Aerts, X. Tu, A. Bogaerts, J. Phys. Chem. C 117 (10) (2013) 4957–4970.

[11] L.L. Alves, A. Bogaerts, V. Guerra, M.M. Turner, Plasma Sources Sci. Technol. 27 (2) (2018) 023002.

[12] W.L. Morgan, B.M. Penetrante, Comput. Phys. Commun. 58 (1) (1990) 127–152.

[13] G.J.M. Hagelaar, L.C. Pitchford, Plasma Sources Sci. Technol. 14 (4) (2005) 722–733, https://bolsig.laplace.univ-tlse.fr/.

[14] N. Dyatko, I. Kochetov, A. Napartovich, A. Sukharev, Eedf: the software package for calculations of electron energy distribution function, http://www.lxcat.net/software/EEDF/, 2015.

[15] https://github.com/aluque/bolos.

[16] A. Tejero-del Caz, V. Guerra, D. Gonçalves, M. Lino da Silva, L. Marques, N. Pinhão, C.D. Pintassilgo, L.L. Alves, Plasma Sources Sci. Technol. 28 (4) (2019) 043001, https://github.com/IST-Lisbon/LoKI.

[17] A. Tejero-del Caz, V. Guerra, N. Pinhão, C.D. Pintassilgo, L.L. Alves, Plasma Sources Sci. Technol. 30 (6) (2021) 065008.

[18] J. Stephens, J. Phys. D, Appl. Phys. 51 (12) (2018) 125203, https://gitlab.com/LXCatThirdParty/MultiBolt.

[19] M. Rabie, C.M. Franck, Comput. Phys. Commun. 203 (2016) 268–277, www.lxcat.net/download/METHES.

[20] S. Biagi, Nucl. Instrum. Methods Phys. Res. A 421 (1) (1999) 234–240, http://magboltz.web.cern.ch/magboltz/.

[21] A.V. Phelps, L.C. Pitchford, Phys. Rev. A 31 (1985) 2932–2949.

[22] H.R. Skullerud, J. Phys. B, At. Mol. Opt. Phys. 2 (6) (1969) 696–705.

[23] www.lxcat.net.

[24] R.D. White, R.E. Robson, B. Schmidt, M.A. Morrison, J. Phys. D, Appl. Phys. 36 (24) (2003) 3125–3131.

[25] R.D. White, R.E. Robson, S. Dujko, P. Nicoletopoulos, B. Li, J. Phys. D, Appl. Phys. 42 (19) (2009) 194001.

[26] Z.L. Petrović, S. Dujko, D. Marić, G. Malović, Ž. Nikitović, O. Šašić, J. Jovanović, V. Stojanović, M. Radmilović-Radjenović, J. Phys. D, Appl. Phys. 42 (19) (2009) 194002.

[27] S. Dujko, R.D. White, Z.L. Petrović, R.E. Robson, Plasma Sources Sci. Technol. 20 (2) (2011) 024013.

[28] T.C. Dias, V. Guerra, Plasma Sources Sci. Technol. 29 (11) (2020) 115003.

[29] G. Colonna, A. Laricchiuta, L. Pietanza, Plasma Phys. Control. Fusion 62 (2020) 014003.

[30] P. Tosi, C. Montesano, S. Quercetti, L.M. Martini, G. Dilecce, J. CO₂ Util. 39 (2020) 101157.

[31] M. Šimek, Z. Bonaventura, J. Phys. D, Appl. Phys. 51 (50) (2018) 504004.

[32] R. Brandenburg, P. Bruggeman, S. Starikovskaia, Plasma Sources Sci. Technol. 26 (2017) 020201.

[33] T.L. Chng, N.D. Lepikhin, I.S. Orel, N.A. Popov, S.M. Starikovskaia, Plasma Sources Sci. Technol. 29 (3) (2020) 035017.

[34] M. Pustylnik, L. Hou, A. Ivlev, L. Vasilyak, L. Couedel, H. Thomas, G. Morfill, V. Fortov, Phys. Rev. E 87 (2013).

[35] M. Matsumoto, T. Nishimura, ACM Trans. Model. Comput. Simul. 8 (1) (1998) 3–30.

[36] T. Nishimura, ACM Trans. Model. Comput. Simul. 10 (2000) 348–357.

[37] http://www.cplusplus.com/reference/random/mt19937_64/.

[38] L.C. Pitchford, L.L. Alves, K. Bartschat, S.F. Biagi, M.C. Bordage, A.V. Phelps, C.M. Ferreira, G.J.M. Hagelaar, W.L. Morgan, S. Pancheshnyi, V. Puech, A. Stauffer, O. Zatsarinny, J. Phys. D, Appl. Phys. 46 (33) (2013) 334001.

[39] O. Klein, S. Rosseland, Z. Phys. 4 (1921) 46–51.

[40] T. Itoh, T. Musha, J. Phys. Soc. Jpn. 15 (9) (1960) 1675–1680.

[41] H.R. Skullerud, J. Phys. D, Appl. Phys. 1 (11) (1968) 1567–1568.

[42] S. Longo, Plasma Sources Sci. Technol. 9 (4) (2000) 468–476.

[43] S. Dujko, Z.M. Raspopović, Z.L. Petrović, J. Phys. D, Appl. Phys. 38 (16) (2005) 2952–2966.

[44] M. Yousfi, A. Hennad, A. Alkaa, Phys. Rev. E 49 (1994) 3264–3273.

[45] I. Reid, Aust. J. Phys. 32 (1979) 231.

[46] V. Vahedi, M. Surendra, Comput. Phys. Commun. 87 (1) (1995) 179–198.

[47] C.B. Opal, W.K. Peterson, E.C. Beaty, J. Chem. Phys. 55 (8) (1971) 4100–4106.

[48] Y.-K. Kim, Atomic and Molecular Processes in Fusion Edge Plasmas, Springer Science, Business Media, New York, 1995.

[49] J.P. Boeuf, E. Marode, J. Phys. D, Appl. Phys. 15 (11) (1982) 2169–2187.

[50] S. Dujko, R.D. White, Z.L. Petrović, R.E. Robson, Phys. Rev. E 81 (2010) 046403.

[51] Z. Raspopovic, S. Sakadzic, S. Bzenic, Z. Petrovic, IEEE Trans. Plasma Sci. 27 (5) (1999) 1241–1248.

[52] J. Mirić, D. Bošnjaković, I. Simonović, Z.L. Petrović, S. Dujko, Plasma Sources Sci. Technol. 25 (6) (2016) 065010.

[53] A.M. Nolan, M.J. Brennan, K.F. Ness, A.B. Wedding, J. Phys. D, Appl. Phys. 30 (20) (1997) 2865–2871.

[54] S. Longo, Plasma Sources Sci. Technol. 15 (4) (2006) S181–S188.

[55] B.M. Penetrante, J.N. Bardsley, L.C. Pitchford, J. Phys. D, Appl. Phys. 18 (6) (1985) 1087–1100.

[56] Z. Petrović, Z. Raspopović, S. Dujko, T. Makabe, Appl. Surf. Sci. 192 (1) (2002) 1–25.

[57] R.D. White, M.J. Brennan, K.F. Ness, J. Phys. D, Appl. Phys. 30 (5) (1997) 810–816.

[58] J. Loureiro, J. Amorim, Kinetics and Spectroscopy of Low Temperature Plasmas, John Wiley & Sons, 2016.

[59] J. Lucas, H.T. Saelee, J. Phys. D, Appl. Phys. 8 (6) (1975) 640–650.

[60] K.F. Ness, R.E. Robson, Phys. Rev. A 34 (1986) 2185–2209.

[61] O₂ on IST-Lisbon data, www.lxcat.net.

[62] Ar on IST-Lisbon data, www.lxcat.net.

[63] G. Gousset, C.M. Ferreira, M. Pinheiro, P.A. Sa, M. Touzeau, M. Vialle, J. Loureiro, J. Phys. D, Appl. Phys. 24 (3) (1991) 290–300.

[64] V. Guerra, J. Loureiro, Plasma Sources Sci. Technol. 8 (1999) 110–124.

[65] S.G. Belostotsky, D.J. Economou, D.V. Lopaev, T.V. Rakhimova, Plasma Sources Sci. Technol. 14 (3) (2005) 532–542.

[66] D.V. Lopaev, E.M. Malykhin, S.M. Zyryanov, J. Phys. D, Appl. Phys. 44 (1) (2010) 015202.

[67] J.-P. Booth, A. Chatterjee, O. Guaitella, J.S. Sousa, D. Lopaev, S. Zyryanov, T. Rakhimova, D. Voloshin, Y. Mankelevich, N. de Oliveira, L. Nahon, Plasma Sources Sci. Technol. 29 (11) (2020) 115009.

[68] J. Loureiro, C.M. Ferreira, J. Phys. D, Appl. Phys. 19 (1) (1986) 17–35.

[69] B. Massabieaux, G. Gousset, M. Lefebvre, M. Pealat, J. Phys. France 48 (11) (1987) 1939–1949.

[70] A. Lo, A. Cessou, P. Boubert, P. Vervisch, J. Phys. D, Appl. Phys. 47 (11) (2014) 115201.

[71] A.W. van de Steeg, T. Butterworth, D.C.M. van den Bekerom, A.F. Silva, M.C.M. van de Sanden, G.J. van Rooij, Plasma Sources Sci. Technol. 29 (11) (2020) 115001.

[72] N₂ on IST-Lisbon data, www.lxcat.net.

[73] R. Chandra, L. Dagum, D. Kohr, R. Menon, D. Maydan, J. McDonald, Parallel Programming in OpenMP, Morgan Kaufmann, 2001.

[74] G. Guennebaud, B. Jacob, et al., Eigen v3.3, http://eigen.tuxfamily.org, 2021.

[75] G.M. Amdahl, AFIPS Conf. Proc. 30 (1967) 483–485.

[76] M.D. Bond, N. Nethercote, S.W. Kent, S.Z. Guyer, K.S. McKinley, in: Proceedings of the 22nd Annual ACM SIGPLAN Conference on Object-Oriented Programming Systems, Languages and Applications, Association for Computing Machinery, New York, NY, USA, 2007, pp. 405–422.